Materials & Design 244 (2024) 113173

Contents lists available at ScienceDirect

Materials & Design

journal homepage: www.elsevier.com/locate/matdes

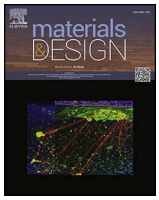

High-throughput strategy to design high entropy alloys with an FCC matrix, $L1_2$ precipitates, and optimized yield stress

Diego de Araujo Santana [a,b,*], Benjamin Ellyson [b], Amy Clarke [b], Kester Clarke [b], Norbert Schell [c], Michael Kaufman [b], Claudio Shyinti Kiminami [d], Francisco Gil Coury [d]

[a] Graduate Program in Materials Science and Engineering, Federal University of São Carlos, Rodovia Washington Luís, km 235 SP-310, 13565-905 São Carlos, São Paulo, Brazil
[b] Colorado School of Mines, 1500 Illinois St., Golden, CO 80401, USA
[c] Institute of Materials Research, Helmholtz-Zentrum Geesthacht, Max-Planck-Str. 1, 21502 Geesthacht, Germany
[d] Department of Materials Engineering, Federal University of São Carlos, Rodovia Washington Luís, km 235 SP-310, 13565-905 São Carlos, São Paulo, Brazil

ARTICLE INFO

Keywords:
High-entropy alloys
Alloy design
Superalloys
Precipitation-hardening

ABSTRACT

This work proposes a methodology for designing high-strength precipitation-hardened high entropy alloys (HEAs) with an FCC matrix and $L1_2$ precipitates. High-throughput solidification calculations were conducted using the CALPHAD method, evaluating 11,235 alloys in the Cr-Co-Ni-Al-Ti system under specific boundary conditions. The acquired information was used to filter the alloys, focusing on alloys exhibiting an FCC+$L1_2$ phase field at 750 °C, a solidification interval narrower than 100 °C, and a solvus temperature under 1100 °C. The filtered alloys were analyzed to estimate their solid solution and precipitation hardening contributions to yield strength, with antiphase boundary energy (APB) assessed using two models. Three alloys were selected for testing the proposed strategy, including one with the highest yield stress and others for comparison. These alloys were produced, processed, and characterized using DSC, synchrotron XRD, SEM, and TEM. The results showed that the desired microstructure was achieved, with the alloys consisting of an FCC matrix and a high-volume fraction of $L1_2$ precipitates. Tensile tests at room temperature, 650 °C, 750 °C, and 850 °C demonstrated that the proposed model predicts well the yield strength trends, demonstrating the potential of the proposed approach for accelerating the discovery and development of novel HEAs with tailored properties.

1. Introduction

Most High Entropy Alloys (HEAs) developed to date were designed to have simple phases, such as body centered cubic (BCC) or face centered cubic (FCC). It was speculated that these solid solutions would be more likely to form because of their high configurational entropies, which could dominate the Gibbs free energy equation [1–3]. This has been demonstrated to be untrue on several occasions [4], the phases in HEAs depend strongly on the elements that are mixed [5]. Besides that, it was speculated that these alloys would inherently possess high solid solution strengthening. As shown by Coury et al. [6,7], this strengthening mechanism has no direct correlation with configurational entropy. Although some of these initial thoughts were proven to be false, single-phase HEAs with interesting properties were discovered. For instance, the ternary CrCoNi alloy shows excellent combination of yield strength and uniform elongation over a wide temperature range [8]. Besides that, its fracture toughness is one of the highest reported to date, even at cryogenic temperature [9,10].

While the early studies focused on producing single-phase HEAs [11], the "second generation" of HEAs has been broadened to include multi-phase compositions. A particular case is that of alloys with an FCC matrix and $L1_2$ precipitates [12–14] or with a BCC matrix and B2 precipitates [15–17], which are being developed to compete with traditional superalloys. These alloys are often named High Entropy Superalloys (HESA) in the literature. The study of precipitation hardened HEAs is relatively recent, and few alloys have been studied so far. Therefore, studies focused on designing new alloys with compositions of even greater potential to reconcile strength, ductility, creep-resistance, oxidation-resistance, and other properties are needed.

Regardless of the intended final microstructure, one of the primary

* Corresponding author at: Graduate Program in Materials Science and Engineering, Federal University of São Carlos, Rodovia Washington Luís, km 235 SP-310, 13565-905 São Carlos, São Paulo, Brazil.
E-mail address: diegodeasantana@ppgcem.ufscar.br (D. de Araujo Santana).

https://doi.org/10.1016/j.matdes.2024.113173
Received 24 May 2024; Received in revised form 9 July 2024; Accepted 18 July 2024
Available online 19 July 2024

challenges in the development of multicomponent alloys with a good combination of properties is to effectively explore the large compositional landscape typical of these systems. For example, superalloys typically contain five or more elements, and over thousands of alloys can be designed when five or more elements are mixed with solute concentrations of 10 % or lower [18]. Hence, the vast array of potential compositions stands as both a significant advantage and a primary challenge in the realm of HEA exploration.

The conventional approach for designing new alloys within a multicompositional space typically follows a sequence of steps. Initially, the strategy involves predicting the equilibrium phases within the alloy system. This process often includes the computation of pseudo-binary or pseudo-ternary diagrams, commonly achieved through techniques like the Calculation of Phase Diagram (CALPHAD) method. These diagrams provide insights into the stability regions of various phases within the compositional space, enabling the identification of suitable compositions for focus. Once the promising compositions are defined, the overall alloy properties are estimated for a specific application after appropriate processing steps.

This approach has its limitations. It relies on fixing two or more elements in a predefined ratio due to the constraints imposed by the two degrees of freedom (DF) on a bidimensional phase diagram. While this method has indeed contributed to the creation of alloys with intriguing properties, there remains a portion of the compositional space that goes unnoticed. For example, consider a system denoted as A-B-C-D. When constructing a pseudo-ternary diagram for this system, the user is compelled to select two species that form a component in a predetermined ratio. The vertices of the pseudo-ternary diagram could be labeled as (AiBj), C, and D, where i and j are arbitrary coefficients representing the proportions between species A and B. The degrees of freedom in this pseudo-ternary system are confined to just two, whereas the practical system inherently possesses three degrees of freedom, or four, if temperature is considered. Consequently, any compositions located beyond the boundaries of the predetermined proportions are disregarded during the analysis. This discrepancy highlights the potential limitations of the usual approach. While it has undoubtedly been instrumental in alloy design, a large unexplored region remains, within the desired compositional space, that these methods fail to capture. The high-throughput approach, although more time-consuming, bridges this gap by enabling effective exploration of any region within a multicompositional space.

In this context, a novel strategy is proposed for designing new alloys with an FCC matrix, $L1_2$ precipitates, and enhanced yield stress. The method integrates high-throughput thermodynamic calculations to screen the multicompositional space and yield stress modeling to predict the strength of the alloys. Specifically, equilibrium solidification calculations were performed within the Cr-Co-Ni-Al-Ti system, using the CALPHAD method through Pandat^{TM} software [19]. A total of 11,235 compositions were analyzed, and a sequence of filtering criteria was applied. Subsequently, the filtered alloys had their yield stress estimated. To assess the proposed methodology, three alloys were selected and prepared by non-consumable arc melting. They were processed and had their microstructure, thermal, and mechanical properties assessed. It is shown that the approach taken provides a promising path for the faster identification and development of new alloys with optimized properties that can be easily extended for other alloy systems.

2. Models

2.1. High-throughput CALPHAD calculations and alloys filtering

Using the CALPHAD method, through Pandat^{TM} software and the PanHEA2020 database, high-throughput equilibrium solidification calculations were performed on given compositional space of the Cr-Co-Ni-Al-Ti system. The concentration ranges and steps used during calculations for each element are presented in the following series of inequalities, all in atomic percentage.

$$\begin{cases} 0 \le x_{Cr} \le 40, \Delta x_{Cr} = 2.5 \\ 0 \le x_{Co} \le 40, \Delta x_{Co} = 2.5 \\ 0 \le x_{Al} \le 15, \Delta x_{Al} = 2.5 \\ 0 \le x_{Ti} \le 15, \Delta x_{Ti} = 2.5 \\ 0 \le x_{Ni} \le 60, \Delta x_{Ni} = - \end{cases}$$

where nickel was set as a balance element. Hereafter, all concentrations are denoted in terms of atomic concentration unless otherwise specified.

The boundary conditions assigned to each element were based on typical values observed in commercial wrought superalloys [20,21] extended to encompass a broader compositional range. The combinations yielded a total of 11,235 different alloys. For each one, the calculation was conducted between the *liquidus* and 500 °C. Upon the completion of these calculations, the data were compiled, and three criteria were employed to filter the alloys, namely:

- The alloy should have a two-phase field FCC+$L1_2$ ($\gamma + \gamma'$) at 750 °C. This criterion was established according to the operating temperature prevalent in most wrought nickel superalloys;
- The alloy should have a single-phase FCC field at high temperature and the *solvus* temperature (T_{Solvus}) should be less than or equal to 1100° C. This was defned to guarantee the alloy's ability to undergo precipitation hardening. Furthermore, the upper threshold was set because some forming operations for wrought superalloys are performed above the solvus temperature, and a high solvus temperature can present challenges for alloy processability;
- The solidification interval ($\Delta T_{Solidification}$) should be less than or equal to 100° C. The upper limit for the solidification interval was defined to minimize chemical segregation during solidification and prevent solidification defects such as porosity and cracks.

The Venn diagram presented in Fig. 1 provides a summary of the number of alloys that fulfilled each of the aforementioned criteria, as well as their intersections. It can be observed that out of the initial 11,235 alloys, only 374 (~3%) satisfied all the criteria.

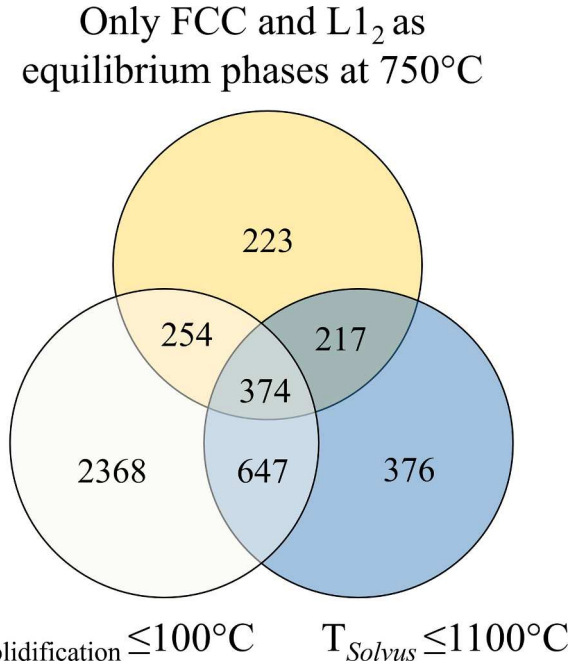

Fig. 1. Venn diagram showing the number of alloys that met each of the three filtering criteria and the intersections between them.

2.2. Yield stress modeling

After the alloys' filtering, the molar fractions, phase compositions, and the $L1_2$ sublattice occupations at 750° C were used as inputs to theoretically predict the yield stress of the alloys.

The yield strength of a polycrystalline alloy (σ_{ys}) is considered to be given by Eq. (1):

$$\sigma_{ys} = (\sigma_{PN} + \sigma_{ss}) + \sigma_{wh} + \sigma_{gs} + \sigma_{pp} \tag{1}$$

where $\sigma_{PN}, \sigma_{ss}, \sigma_{wh}, \sigma_{gs}, \sigma_{pp}$, are the Peierls-Nabarro resistance, solid solution, work hardening, grain size, and precipitation hardening contributions to the yield strength, respectively. Each of these terms are detailed in the following paragraphs in the context of alloys with FCC matrix and $L1_2$ precipitates. As will be discussed, σ_{PN} and σ_{wh} can be disregarded in the theoretical estimation of σ_{ys}. Although σ_{gs} is relevant for the total strength of the material, it should be much less relevant for the compositional screening, considering alloys with similar grain size.

The lattice resistance or Peierls–Nabarro (PN) component is often considered coupled with the solid solution strengthening, since it is not possible to evaluate the former alone in a matrix containing solute atoms. As will be shown later in this work, Varvenne's model for solid solution strengthening predicts a zero stress for a pure metal. Therefore, it only estimates the solid solution contribution alone. However, the magnitude of PN in FCC metals is negligible when compared with the other contributions to yield stress [22].

The work-hardening contribution is proportional to $Gb\sqrt{\rho}$ where G is the shear modulus, b is the Burgers vector length, and ρ is the dislocation density [22]. The shear modulus and lattice parameter of the FCC matrix in superalloys span in the range of 70–85 GPa [23–25], and 0.352–0.366 nm [26], respectively. Since superalloys should be aged to achieve their best combination of properties, recovery and recrystallization take place during the aging treatment, leading to a low dislocation density. Hence, the work-hardening contribution to yield strength is in the range of 2–4 MPa for a typical dislocation density of $\sim 10^{10}$ m^{-2}.

Superalloys are often applied at homologous temperature over 0.5, where creep is an operative deformation mechanism. Consequently, a fine grain size material is unsuitable for high temperature applications. The optimal grain size in polycrystalline wrought superalloys is argued to be in the range of 30–50 μm [20]. Experimental data shows that the room-temperature Hall-Petch locking parameter of wrought superalloys typically spans from 700 to 1000 MPa.μm^{½} [27,28]. Therefore, the grain size contribution to yield strength, given by $k/\sqrt{d}$, is approximately 150 MPa, depending on the exact final grain size. More importantly, in this work, this contribution should be approximately the same for all compositions given that the final grain size is similar.

The σ_{ss} and σ_p contributions to yield strength are discussed in more detail in the following paragraphs.

2.3. Solid solution hardening contribution

The theoretical modeling of the solid solution hardening contribution in multicomponent systems is relatively recent. For example, in most works related to superalloy design, semi-empirical relationships have been used to estimate the σ_{SS} value [29,30]. In the context of high entropy alloys, Varvenne et al [31,32] proposed a mechanistic model to deal with concentrated solutions. In this model, each component of the solid solution can be considered as a "solute" embedded in an "average solvent", with the latter having the average properties of the solution. The "solutes" lead to local compositional fluctuations with respect to the average solvent and interact with the strain field of the dislocations, offering a barrier to dislocation motion. In Varvenne's theory, the zero-temperature flow stress and the energetic barrier for dislocation glide are given by Eqs. (2) and (3), respectively,

$$\tau_{ss,0} = 0.051\alpha^{-\frac{1}{3}} G\left(\frac{1+\nu}{1-\nu}\right) f_1(w_c)\left(\frac{\sum_n x_n \Delta\overline{V}_n^2}{b^6}\right)^{\frac{2}{3}}, \tag{2}$$

$$\Delta E_b = 0.274\alpha^{\frac{1}{3}} Gb^3\left(\frac{1+\nu}{1-\nu}\right)^{\frac{2}{3}} f_2(w_c)\left[\frac{\sum_n x_n \Delta\overline{V}_n^2}{b^6}\right]^{\frac{1}{3}}, \tag{3}$$

where b, G and ν are the dislocation Burgers vector length, the shear modulus, and the Poisson ratio of the FCC matrix, respectively. The $f_1(w_c)$ and $f_2(w_c)$ terms are numerical coefficients, related to dislocation core structures, which are nearly constant at 5.70 and 0.35, respectively. The x_n and $\Delta\overline{V}_n$ terms are the atomic concentration of the nth element in the FCC matrix and the average misfit volume caused by the element nth in the solid solution. The latter is given by $\Delta\overline{V}_n = V_n - \overline{V}$, where V_n is the apparent volume of the nth element in the solid solution and $\overline{V}$ is the average atomic volume of the matrix. The parameter α is a dimensionless constant related to the dislocation line tension, which is considered as $\Gamma = \alpha G b^2$. For several FCC metals, atomistic simulations showed that $\alpha = 1/8$ is accurate [33]; thus, it was used in this work.

The solid solution contribution in a multi-element system can finally be calculated using Equations 4 or 5, which also consider the effects of temperature (T) and the applied strain rate ($\dot{\varepsilon}$) on σ_{ss}.

$$\sigma_{ss}(T,\dot{\varepsilon}) = M\tau_{ss,0}\left[1 - \left(\frac{k_B T}{\Delta E_b}\ln\frac{\dot{\varepsilon}_0}{\dot{\varepsilon}}\right)^{\frac{2}{3}}\right]\frac{1}{M}\frac{\sigma_y}{\sigma_{y,0}} \leq 0.3 \tag{4}$$

$$\sigma_{ss}(T,\dot{\varepsilon}) = M\tau_{ss,0}\exp\left(-\frac{1}{0.51}\frac{k_B T}{\Delta E_b}\ln\frac{\dot{\varepsilon}_0}{\dot{\varepsilon}}\right)\frac{1}{M}\frac{\sigma_y}{\sigma_{y,0}} \geq 0.6 \tag{5}$$

where M is the Taylor factor, k_B the Boltzmann constant, and $\dot{\varepsilon}_0$ a reference strain rate. Following Varvenne, $\dot{\varepsilon}_0$ was set as $10^4 s^{-1}$. In a non-zero temperature, the quantities $\tau_{ss,0}$ and ΔE_b in Eqs. (2) and (3) are computed using the elastic constants G and ν at a given temperature T.

As can be seen in the previous Eqs. (2)–(5), to apply the model, some of the alloy's properties must be known in advance, such as the elastic constants and the lattice parameter of the solid solution. For the former, the values of G and ν for each alloy in the Cr-Co-Ni-Al-Ti system were estimated using the rule of mixture ($G = \sum_n x_n G_n$ and $\nu = \sum_n x_n \nu_n$, respectively) and the elastic constants for Ni, CoNi, and CrCoNi alloys reported by Wu et al. [8], and the empirical relationship proposed by Varvenne et al. [34]. These relationships are given in the Eqs. (6) and (7). The effect of titanium on the elastic properties was neglected, but this is reasonable since titanium strongly partitions to the $L1_2$ phase. For instance, the maximum titanium concentration in the FCC phase at 750° C in the filtered alloys was only 3.7 %.

$$G = (76x_{Ni} + 92x_{Co} + 93x_{Cr})(1 - 1.51x_{Al}) \tag{6}$$

$$\nu = 0.31x_{Ni} + 0.27x_{Co} + 0.32x_{Cr} + 0.2x_{Al} \tag{7}$$

The atomic volume of the elements in the FCC matrix were calculated using the Effective Atomic Radii for Alloys Strength (EARS) method [7]. The values were previously estimated [35], and they are summarized in Table 1. The average atomic volume of the matrix can be calculated assuming valid Vergard's law, i.e., $\overline{V} = \sum_n x_n V_n$.

Lastly, the Burgers vector can be established from the relationship between the average atomic volume and lattice parameter of an FCC solid solution ($\overline{V} = a^3/4$), being equal to $b = \left(\sqrt{2}\,\overline{V}\right)^{1/3}$.

Table 1
Atomic volume of Cr-Co-Ni-Al-Ti used for calculating the solid solution hardening contribution in this work. Extracted from [35].

Element	Ni	Cr	Co	Al	Ti
Atomic volume, V_n(Å^3)	10.94	12.86	11.52	13.52	14.48

To summarize, the equilibrium composition of the FCC phase at 750° C, for each filtered alloy, was employed as input for estimating the solid solution hardening contribution using Varvenne's model. The elastic constants of the FCC matrix were computed using Eqs. (6) and (7). The average atomic volume of the matrix was calculated using the values presented in Table 1. A Taylor factor for a untextured FCC polycrystal ($M = 3.06$) was utilized in Eq. (5) for the calculations of σ_{ss}.

2.4. Precipitation hardening contribution

In a matrix containing coherent ordered precipitates, the dislocations motion along their slip planes occurs by groups [36]. In the case of an FCC/$L1_2$ microstructure, the dislocations slip in pairs, separated by an equilibrium distance w [37]. While the leading dislocation shears the precipitates, creating an antiphase boundary (APB), the trailing dislocation restores the perfect order in the precipitates after its passage.

In underaged alloys, the distance between the dislocations is significantly greater than the average precipitate radius. In such case, the dislocations in the pair are referred to be weakly-coupled and the precipitation hardening contribution increases as the mean particle size increases. Conversely, in overaged alloys, the separation w is smaller than the mean precipitates diameter and the dislocations are referred to be strongly coupled. Under this condition, the trailing dislocation starts to restore the order within the faulted precipitate before the leading dislocation leaves the particle. When w is smaller than the mean precipitate radius the leading dislocation exits the precipitates without encounters the maximum resistive force provided by the precipitate. Consequently, the precipitation hardening contribution decreases as the precipitates coarse [38].

The peak strength due to ordered particles occurs for a precipitate radius that lies between the weak and strong couple configuration, and it can be estimated using Eq. (8) [39].

$$\sigma_{pp,o}^{peak} = M\left[0.81\frac{\chi_{APB}}{2b}\left(\frac{3\pi f}{8}\right)^{1/2}\right]. \tag{8}$$

where M is the Taylor factor, χ_{APB} is the antiphase boundary energy, b is the magnitude of Burgers vector, and f is the volume fraction of $L1_2$ precipitates. As can be seen, this equation is independent of precipitates radius, which makes it easier to implement since it does not depend upon kinetic factors.

As shown by Ardell [39], the Eq. (8) is not particularly accurate for predicting quantitatively the peak strength of most alloys. One possible reason suggested by this author is the influence of finite particle size in the precipitate-dislocation interaction, which is not considered in its derivation. Nonetheless, experimental data from mechanical tests of different superalloys shows excellent correlation between $\Delta\tau_{c,max}/f^{1/2}$ and χ_{APB} [39], where $\Delta\tau_{c,max}$ is the maximum precipitation hardening contribution to yield stress measured experimentally. Therefore, for design purposes the previous equation should prove to be satisfactory.

It is worth mentioning that some other precipitation hardening mechanism may play a significant role in the precipitation hardening contribution to yield stress, such as coherency and modulus hardening [22]. However, in FCC/$L1_2$ microstructure the order strengthening tends to dominate σ_{pp}, leading to precipitation hardening contribution at peak aging condition being, approximately, $\sigma_{pp,o}^{peak}$.

In this context, the equilibrium molar fraction of the $L1_2$ phase, alongside the compositions of both the FCC and $L1_2$ phases at 750 °C, were employed to assess the magnitude of σ_{pp}^{peak}. Given the similar densities of the FCC and $L1_2$ phases, approximating the volume fraction of $L1_2$ to its molar fraction introduces minimal error. The estimation of the Burgers vector length utilized the FCC composition as its input (as discussed previously), whereas the $L1_2$ composition was utilized to compute the APB energy, as detailed next.

2.5. Antiphase boundary energy

As can be noted in Eq. (8), the APB energy is a key parameter for design precipitation hardened alloys with optimized yield stress. Although understanding the effect of each element on the χ_{APB} of the $L1_2$ phase is highly desirable, obtaining such knowledge has proven to be challenging experimentally, analytically, and computationally.

Experimentally, the most used technique to estimate the value of χ_{APB} is through the measurement of the distance between dislocations by means of TEM analyses and estimation of APB energy magnitude by using elasticity theory [40–42]. Another way of estimating the value of χ_{APB} is by fitting the precipitation's contribution extracted from yield stress of underaged alloys [25,39,43]. Aside from the challenges associated with both methodologies, their major disadvantage resides on the need to produce the alloy with the composition of the $L1_2$ phase of interest to assess the APB energy magnitude. Therefore, the use of analytical or computational methods that allow predicting the χ_{APB} in advance proves to be extremely relevant in the context of designing new alloys.

Flinn [44] formulated a nearest-neighbor bonding model to predict the antiphase boundary energy within the $L1_2$ structure considering the first nearest neighbor atoms. More generalized models for APB energy estimation were later developed [45–47]. However, these analytical models often involve parameters that cannot be estimated through experimental means. To overcome this issue, Miodownik and Saunders [48] proposed a method to estimate these parameters, up to some degree, by the CALPHAD method. Strictly speaking, the Miodownik and Saunders's model is applicable only for binaries alloys. However, it is frequently extrapolated for high-order systems in the literature [49–52].

Dodaran et al. [53] carried out atomistic calculations to systematically assess the alloying effects of Ti, Cr, Co on multicomponent Cr-Co-Ni-Al-Ti system. The effect of these elements on APB was studied at different temperatures (227 °C – 1027 °C). Following Crudden et al. [52], an empirical equation (Eq. (9)) was proposed to calculate the antiphase boundary energy of the $L1_2$ phase.

$$\chi_{APB} = \chi_{APB}^{Ni_3Al} + \sum_{i=1}^{n} K_i x_i + F_1 x_{Ti} x_{Cr} + F_2 x_{Ti} x_{Co} + F_3 x_{Cr} x_{Co} + H x_{Ti} x_{Cr} x_{Co} \tag{9}$$

where x_i is the atomic percentage of element i in the $L1_2$ structure, and K_i, F_1, F_2, F_3, and H are empirical coefficients. As can be noted, interaction terms between the species are also included in this equation. The values of the coefficients for the different temperatures are presented in Table 2. These values were determined by least square minimization method using the Eq. (9) and the computational data. The authors proposes that an appropriate value for $\chi_{APB}^{Ni_3Al}$ is 195 ± 5 mJ/m^2, which was determined experimentally through the TEM approach in another study [40].

Recently, Vamsi and Karthikeyan [54] proposed an environment dependent nearest neighbor bond (EDNNB) model for estimating the APB energy on {1 1 1} planes in multicomponent Ni-base superalloys. Using CALPHAD calculations, the authors showed that the nickel sublattice is primarily composed of Ni and Co atoms. They also argued that

Table 2
Contribution coefficient for antiphase boundary energy at different temperatures for each element (ki) and interaction factors between different solutes (Fi). Coefficients have units in mJ/m^2.

Coefficients (mJ/m^2)	227 °C	427 °C	627 °C	827 °C	1027 °C
k_1(Ti)	8.862	8.196	8.011	7.795	7.56
k_2(Cr)	−4.497	−4.793	−5.256	−6.184	−7.962
k_3(Co)	−1.229	−1.423	−1.574	−1.838	−2.41
F_1(Ti-Cr)	0.8166	0.6286	0.5223	0.6641	0.8702
F_2(Ti-Co)	0.0916	0.0954	0.0628	0.0634	0.1109
F_3(Cr-Co)	−4.337	−4.44	−5.266	−5.681	−5.532
H(Ti-Cr-Co)	0.3211	0.3724	0.4626	0.4975	0.4792

previous DFT studies have shown that substituting Ni with Co has a minimal effect on APB (1 1 1) energies. Therefore, they proposed that the composition of the Al sublattice controls the overall APB energy. Since Al-Al, Al-Ta, Al-Cr, Ti-Cr, Ti-Ti, and Ta-Ta interactions account for about 80 % of forbidden bonds created after APB formation in most Ni-superalloys, the authors proposed the Eq. (10) to calculate the APB energy in these multicomponent systems,

$$\chi_{APB} = \alpha \left[\begin{pmatrix} x_{Al}^2 & x_{Ti}^2 & x_{Ta}^2 & 2x_{Al}x_{Ti} & 2x_{Al}x_{Ta} & 2x_{Al}x_{Cr} & 2x_{Ti}x_{Cr} \end{pmatrix} \begin{pmatrix} \Gamma_{AlAl} \\ \Gamma_{TiTi} \\ \Gamma_{TaTa} \\ \Gamma_{AlTi} \\ \Gamma_{AlTa} \\ \Gamma_{AlCr} \\ \Gamma_{TiCr} \end{pmatrix} \right],$$

$$\Gamma_{ij} = \Gamma_{ij}^0 + \begin{pmatrix} x_{Ti} & x_{Ta} & x_{Cr} & x_{Mo} & x_{Nb} & x_{Ni} & x_W \end{pmatrix} \begin{pmatrix} \eta_{ij,Ti} \\ \eta_{ij,Ta} \\ \eta_{ij,Cr} \\ \eta_{ij,Mo} \\ \eta_{ijl,Nb} \\ \eta_{ij,Ni} \\ \eta_{ij,W} \end{pmatrix},$$

$$\alpha = \frac{1}{\sum p_{ij}}. \tag{10}$$

where x_i is the concentration of species i in the Al-sublattice, while Γ_{ij} represents the APB energy on {1 1 1} plane with a specific combination of interaction across the APB. Here, ij denotes the type of bonding that is gained upon the creation of APB. Additionally, Γ_{ij}^0 is a penalty term that arises due to a specific bonding type in Ni_3Al structure. The coefficient $\eta_{ij,i}$ is a resultant coefficient that accounts for the effect of i at different distances from the fault, and α is a scaling factor used to account for any violations that are ignored in the calculation. The probability of having a violation of type ij across the fault is denoted by p_{ij}, and $\sum p_{ij}$ represents the summation of probabilities of the seven Γ_{ij} terms. The values of Γ_{ij}^0 and $\eta_{ij,k}$ were determined using DFT calculation and they are summarized in the Table 3.

Different works that focused on investigating the effect of a ternary specie on the Ni_3Al structure, by ab initio methods, were reported in the literature [52,55–57]. However, given the multicomponent nature of superalloy systems, this work exclusively assessed Dodaran and Vamsi's models [53,54] – which were specifically proposed to be extrapolated for multicomponent systems – to estimate the APB energy. As will be discussed latter, the former model was chosen for APB calculations.

2.6. Alloys selection

After mathematical modeling of solid-solution, antiphase boundary energy, and precipitation hardening strengthening, the alloys were ranked in descending order of the summation $\sigma_{ss} + \sigma_{pp}$. To assess the effectiveness of the proposed methodology, three alloys were carefully chosen. One to display the most promising yield stress, serving as a benchmark, while the other two were selected to validate the model's predictive capacity. To assess the effect of APB on the yield stress, one alloy was selected to have a similar volume fraction of precipitates with the benchmark, but a lower antiphase boundary energy. To test the effect of volume fraction of precipitates, another composition was chosen to have a much higher volume fraction of precipitates. Table 4 summarize the information related to the selected alloys with FCC and $L1_2$ phases as equilibrium phases at 750 °C.

3. Materials and methods

Two ingots of approximately 100 g of each selected alloy were prepared using commercially pure elements (purity of 99 % or above) in a non-consumable arc melter furnace under argon atmosphere. The raw elements were melted and flipped at least three times to enhance the chemical homogeneity and the molten alloy was poured into a cylindrical copper mold of 12.6 mm diameter and 90 mm height. The arc-melted ingots were homogenized at 1200 °C for 12 h and water quenched. The cylindrical samples were cold rolled in multiple passes until a thickness of 4.9 mm (total reduction of ~ 60 %) was achieved followed by a recrystallization treatment at 1200 °C for 1 h. The recrystallized sheets were cold rolled again until a final thickness of about 1 mm (total reduction of ~ 90 %) was achieved.

Samples from the cold-rolled sheets were solution-treated at 1200 °C for 1 h and aged at 750 °C for 0.5, 2, 4, 10, 25, 50, 100, and 200 h. All samples were quenched to room temperature into water. For heat-treatment, the samples were wrapped in stainless steel foils to reduce the superficial oxidation. The samples were metallographically prepared using an automated grinding and polishing system. The Vickers hardness as a function of aging time was measured at room temperature using a micro indentation hardness testing system following the ASTM-E384 standard [58]. Sixteen measurements were made on each sample. A load of 500 g and a dwell time of 10 s were used during the tests.

Thermal analysis was performed on the samples in the aged condition using a differential scanning calorimetry (DSC) Netzsch 404 under an argon flow atmosphere of ~ 1 bar. The samples were heated up to 1000 °C with a constant heating rate of 10 °C/min.

The microstructure of the sample at the different conditions was characterized by Scanning Electron Microscope (SEM) using a TESCAN S8252G, and Transmission Electron Microscope using a TECNAI G2 F20, operating at 200 kV.

High energy X-ray diffraction (HEXRD) measurements, in the transmission mode, were conducted to identify the crystalline phases at the P07 beam line of the synchrotron radiation facility PETRA III at the Deutsches Elektronen-Synchrotron (DESY). The X-ray beam had a cross section of 1x1 mm^2 and a fundamental photon energy of 87.1 keV (0.14235 Å).

Tensile test specimens were cut from the cold rolled sheets by electrical discharge machining (EDM) with their axes parallel to the rolling direction. The specimens were given a final solution-treatment at 1200 °C for 1 h, quenched into water, and aged for 100 h at 750 °C. This aging time was determined based on hardness measurements carried out previously. At 100 h of aging, all samples were found to have reached the peak aging condition. Tensile tests were performed at room temperature, 650, 750 and 850 °C in a Material Testing System (MTS) Servohydraulic Test System at strain rate of 10^{-3} s^{-1}. The samples were

Table 3
Penalty terms (Γ_{ij}^0) and environment strength coefficients ($\eta_{ij,k}$) for ij violation in the Al-sublattice. All terms are given in units of mJ/m^2.

ij	Γ_{ij}^0	$\eta_{ij,Ti}$	$\eta_{ij,Ta}$	$\eta_{ij,Cr}$	$\eta_{ij,Mo}$	$\eta_{ij,Nb}$	$\eta_{ij,Ni}$	$\eta_{ij,W}$
AlAl	189.0	97.2	163.9	82.6	216.5	162.6	−23.6	247.5
AlTi	353.9	96.1	224.2	116.9	312.7	197.1	−109.5	367.0
AlTa	511.8	129.4	159.4	−36.0	132.5	92.6	−222.0	212.7
AlCr	259.8	50.5	49.0	114.5	−14.6	35.7	−108.8	29.2
TiTi	521.5	221.3	284.9	286.4	263.8	271.2	139.3	317.6
TiCr	390.9	17.0	−46.8	50.5	−151.3	−82.4	−76.8	−124.2
TaTa	688.8	111.7	1.3	13.9	−121.9	8.3	99.5	−161.6

Table 4
Solid solution hardening contribution to yield strength (σ_{ss}), equilibrium molar fraction of $L1_2$ phase at 750 °C (f_{L1_2}), antiphase boundary energy (χ_{APB}), and precipitation hardening contribution to yield strength (σ_{pp}^{peak}) for $Cr_{20}Co_{12.5}Ni_{60}Al_{2.5}Ti_5$, $Cr_{22.5}Co_{10}Ni_{60}Al_5Ti_{2.5}$, and $Cr_{20}Co_{17.5}Ni_{50}Al_{12.5}$ alloys.

Rank position	Alloy	σ_{SS}(MPa)	f_{L1_2}	χ_{APB}(mJ/m^2)	σ_{pp}^{peak}(MPa)	$\sigma_{SS}+\sigma_{PP}^{peak}$(MPa)
1	**$Cr_{20}Co_{12.5}Ni_{60}Al_{2.5}Ti_5$**	216	0.35	329	1035	1251
27	**$Cr_{22.5}Co_{10}Ni_{60}Al_5Ti_{2.5}$**	211	0.34	209	645	856
53	**$Cr_{20}Co_{17.5}Ni_{50}Al_{12.5}$**	206	0.49	158	583	790

induction heated to the target temperatures. A high temperature contact extensometer was used for strain measurements. Triplicate tests were performed in each temperature. The yield strength of the alloys was determined as the stress at which 0.2 % plastic strain occurs, often called 0.2 % offset yield strength.

4. Results and discussion

As first step of yield strength modeling, the Dodaran and Vamsi's model for APB energy estimation were critically assessed using the data of the filtered alloys. The former predicts unrealistic negative values for χ_{APB} when the alloys are Ti-absent. This is mainly justified by a strong penalty term due to Cr-Co interaction and by the fact that the reported coefficients were estimated only for composition of the $L1_2$ phase with Ti concentration in the range of 1–15 %. Therefore, for Ti-free alloys, the interaction terms in Dodaran's model were neglected during the calculations. Fig. 2 shows a favorable correlation between the two APB energy models. However, it is notable that Vamsi's model yields higher χ_{APB} values, approximately ~ 125 mJ/m2 higher than those predicted by Dodaran's model. Notably divergent from this relationship are the datasets corresponding to alloys free of titanium and aluminum. This deviation can be rationalized by considering the Ti concentration range analyzed by Dodaran et al [53], as previously mentioned, and by the fact that all studied alloys presented aluminum in its composition.

Irrespective of the APB models employed, both models converged in the same direction during the process of APB estimation. Since Dodaran's model yielded estimated values more closely to those experimentally measured by using other methods [39,59–61], it was the preferred choice for this study.

Fig. 3 displays the solid solution and precipitation hardening contribution of the filtered alloys. The color and size of the data points correlate to the magnitude of the APB energy and the molar fraction of the $L1_2$ phase, respectively. While the σ_{SS} ranges from 140-240 MPa, the σ_{pp} values exhibit a broader span, ranging from a few tenths of megapascals, up to as high as 1035 MPa for the one of the selected compositions. Overall, the summation $\sigma_{SS}+\sigma_p$ lies in the range of 500–1000 MPa.

While numerous alloys exhibit a substantial molar fraction of $L1_2$ phase, it is noteworthy that those boasting the highest APB energy also display the highest precipitation hardening component. This can be rationalized by the linear correlation of σ_{pp} with APB energy, in contrast to the square root dependence on the volume fraction of precipitates, as indicated by Eq. (8).

The filtered alloys had a maximum nominal titanium concentration of 5 %. Several works [52,55–57] shows that titanium is amongst the elements that substantially raise the APB energy. An increase in the titanium concentration tends to lower the liquidus temperature and, consequently, may widen the solidification interval. Furthermore, an excessive addition of titanium might stabilize other phases, such as the η (Ni_3Ti), which is generally considered deleterious to mechanical properties. This prevents the presence of a stability region limited to only FCC+$L1_2$ phases. It is important to highlight, however, that alloys with nominal titanium concentrations greater or equal to 7.5 % were filtered primarily because these compositions lacked a single-phase FCC field. Despite Ni exhibiting a solubility of over 10 % Ti at high temperatures [62], the CALPHAD calculation indicates that the solubility limit of Ti decreases in the presence of the other elements in the system investigated. Thus, to increase the titanium concentration and consequently enhance the APB and yield stress of precipitation hardened alloys, it is advisable to explore other systems that tend to stabilize an FCC single phase field at high temperatures even for high Ti concentrations.

The ellipses in Fig. 3 indicate two different datasets of alloys with a nominal Ti concentration equal to 5 %. One presents an aluminum concentration of 5 %, whereas in the other the concentration of this element is 2.5 %. The alloys in the former present a higher molar fraction of precipitates in comparison to alloys in the latter. This is justified by the fact that both Al and Ti are $L1_2$ formers. However, since these elements tend to occupy the same sublattice in the $L1_2$ phase, an increase the titanium content, for example, must be balanced with a decrease in aluminum concentration. Analysis of the data reveals that, for the Cr-Co-Ni-Al-Ti system, the combined summation of titanium and

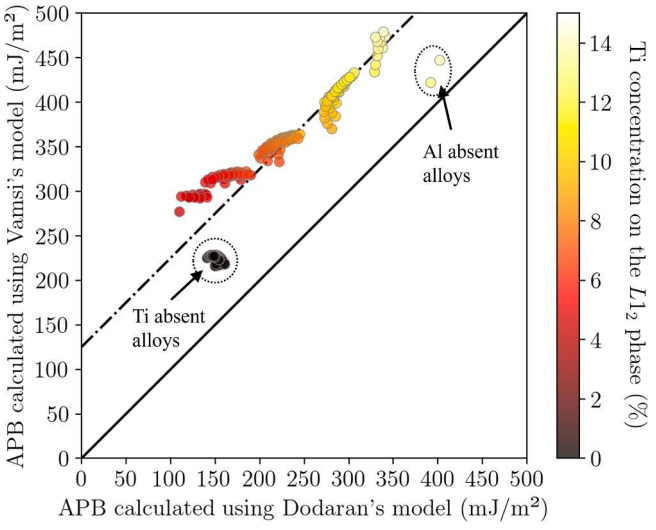

Fig. 2. Antiphase boundary energy calculated for the filtered alloys using Dodaran and Vamsi's models.

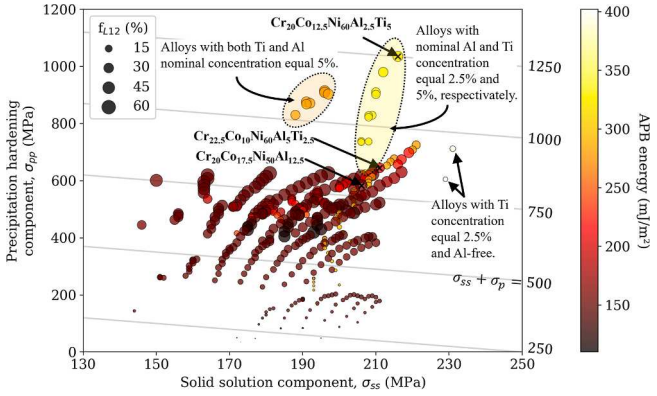

Fig. 3. Solid solution and precipitation hardening contribution to the yield strength of the filtered alloys in this work. The size of the data points scales with the equilibrium molar fraction of the $L1_2$ phase at 750 °C, while the colors indicate the magnitude of the calculated APB energy.

aluminum reaches a saturation limit of approximately 22 % in the $L1_2$ phase. The remaining 3 % of the Al-sublattice is primary occupied by chromium. This sets the following constraint on the maximum nominal Ti concentration: $x_{Ti}^{max} = 0.22 f_{L12} - x_{Al}$. It is important to note that this equation holds true solely when the volume fraction of $L1_2$ is higher than 4.54 x_{Al} and $x_{Al} < 0.22$.

As shown, the integration of thermodynamic calculations with the modeling of the targeted properties leads to a better understanding and it is a valuable tool in alloy design.

Fig. 4 shows the thermodynamic calculation for the three selected alloys, $Cr_{20}Co_{12.5}Ni_{60}Al_{2.5}Ti_5$, $Cr_{22.5}Co_{10}Ni_{60}Al_5Ti_{2.5}$, and $Cr_{20}Co_{17.5}Ni_{50}Al_{12}$, displaying the molar fraction of equilibrium phases as a function of temperature. As the aluminum concentration in the alloys increases, the stability of the single-phase FCC field also increases. Since metal forming operations in some wrought superalloys are carried out above the solvus temperature, a wider FCC field has the advantage of expanding the processability window. On the other hand, while the two alloys containing Ti present a wide field of FCC+$L1_2$ as equilibrium phases, this field in the Ti-absent alloy is much narrower. A broader FCC+$L1_2$ field enables the alloys to operate over a wider temperature range without the formation of additional phases that could adversely affect mechanical properties.

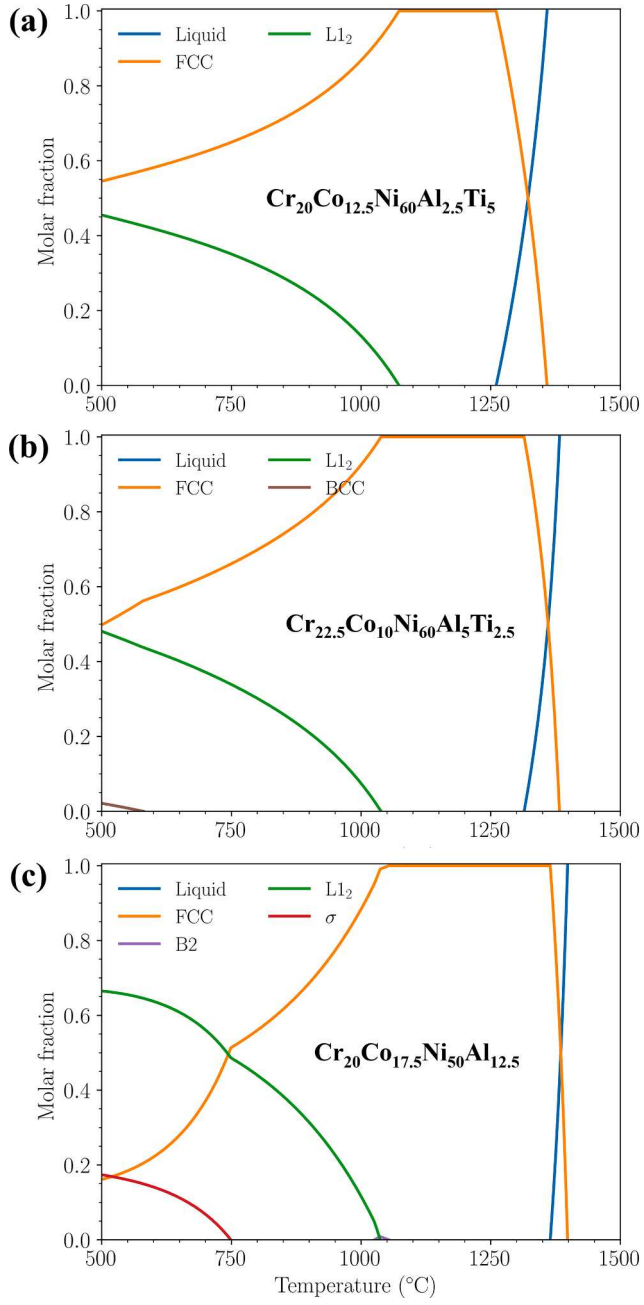

Fig. 4. Thermodynamic calculation displaying the molar fraction of equilibrium phases as a function of temperature for a) $Cr_{20}Co_{12.5}Ni_{60}Al_{2.5}Ti_5$, b) $Cr_{22.5}Co_{10}Ni_{60}Al_5Ti_{2.5}$, and c) $Cr_{20}Co_{17.5}Ni_{50}Al_{12.5}$ alloys.

The results of the thermal analyses carried out on samples of the selected alloys aged at 750 °C are shown in Fig. 5. The *solvus* temperature was determined as the final temperature of the endothermic reaction of FCC+$L1_2$ → FCC, whereas the solidus was determined as the start temperature of the endothermic melting peak of the alloys. The results predicted by thermodynamic calculations are presented in the table inset of the figure. As can be seen, there is a good agreement between the values measured experimentally and those calculated by the CALPHAD method. Since the final temperature of the endothermic peak is uncertain, it is not possible to determine the liquidus accurately. However, it can be noted that the width of the melting peaks scales with the width of the calculated solidification interval.

SEM images of the cold-rolled sheets after solution treatment at 1200 °C for 1 h plus water quenching is shown in the left column of Fig. 6. These images were acquired using the SEM backscattered electron detector (BSE). Annealing twins and some inclusions elongated along the rolling direction can be observed in the images. In the two titanium containing alloys, the inclusions were identified as titanium nitride (TiN). This inclusion is commonly observed in most superalloys since Ti is a strong nitride former element and tends to react with the nitrogen dissolved in the melt [63]. On the other hand, Al-N rich inclusions were observed in the Ti-free alloy. The inclusions are small and have a low volume fraction. From a mechanical property's standpoint, these defects might have some impact on the late stages of deformation, decreasing the ductility of the alloy.

Dark-field TEM images of the solution treated alloys and their respective diffraction pattern (shown inset) are presented in the right column of Fig. 6. The colors of the patterns were inverted to improve the clarity of the superlattice reflections. The TEM images were acquired using the superlattice reflection of $L1_2$ phase close to arbitrary low index zone axis. The approximate radius of these particles is also presented inset each TEM image. The formation of $L1_2$ precipitates upon fast cooling is often observed for nickel superalloys with relative high equilibrium fraction of $L1_2$ phase at high temperature.

High resolution SEM images taken from the interior of randomly

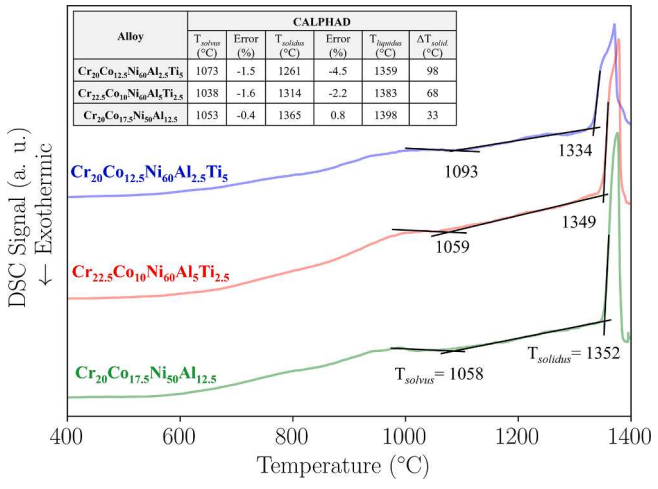

Fig. 5. DSC curves of $Cr_{20}Co_{12.5}Ni_{60}Al_{2.5}Ti_5$, $Cr_{22.5}Co_{10}Ni_{60}Al_5Ti_{i2.5}$, and $Cr_{20}Co_{17.5}Ni_{50}Al_{12.5}$ alloys heated using a heating rate of 10 °C/min. The errors shown in the table inset were calculated using Kelvin scale as the CALPHAD method employs this scale during calculations.

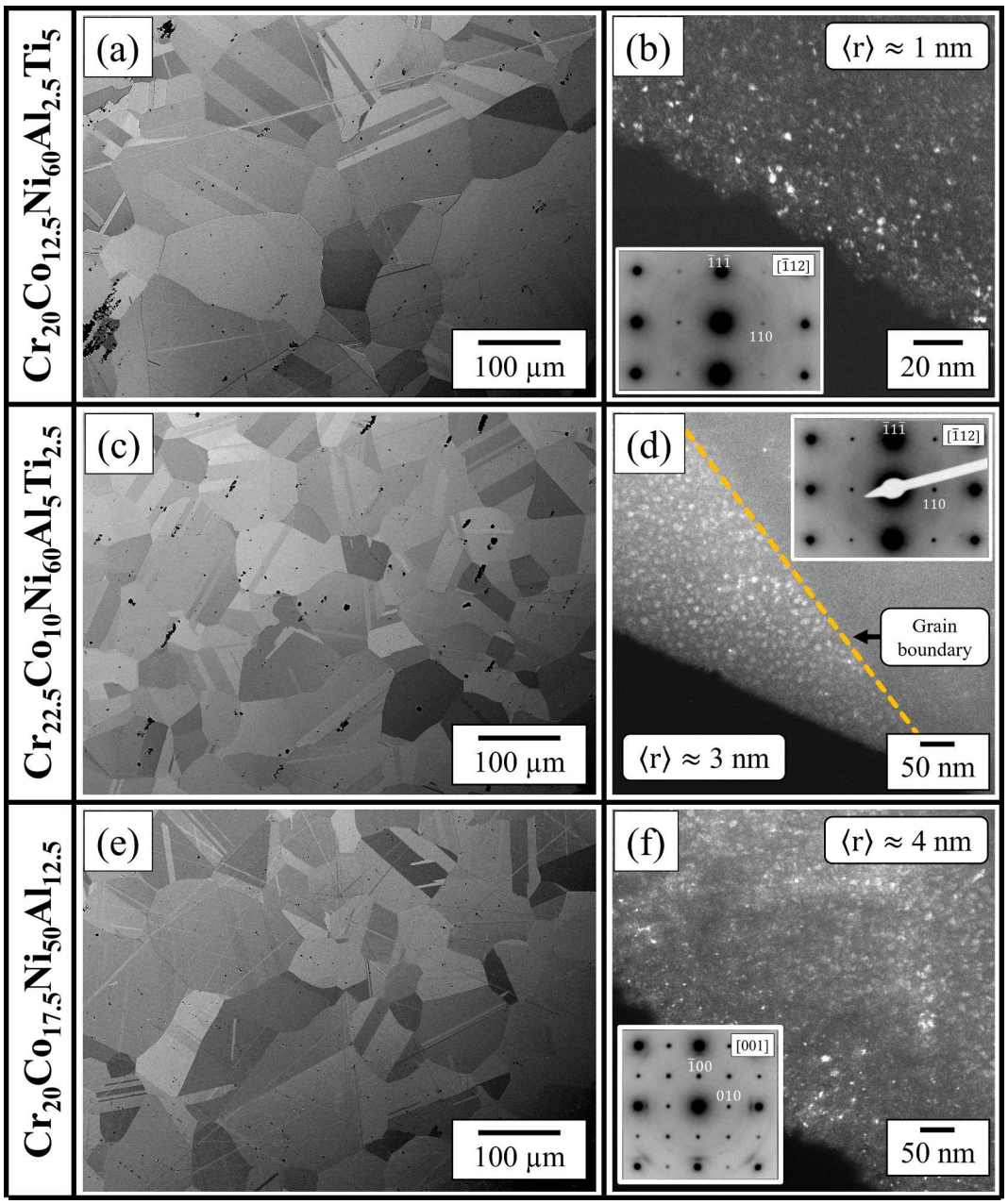

Fig. 6. Microstructural characterization of the produced alloys in the solution treated condition (1 h at 1200 °C plus water quenching). The left column shows SEM images, acquired using backscattered electron, of (a) $Cr_{20}Co_{12.5}Ni_{60}Al_{2.5}Ti_{5,}$ (c)$Cr_{22.5}Co_{10}Ni_{60}Al_5Ti_{2.5,}$ and (e) $Cr_{20}Co_{17.5}Ni_{50}Al_{12.5}$ alloys. The right column shows Dark-Field TEM images, acquired using $L1_2$ superlattice reflection, of (b) $Cr_{20}Co_{12.5}Ni_{60}Al_{2.5}Ti_{5,}$ (d) $Cr_{22.5}Co_{10}Ni_{60}Al_5Ti_{2.5,}$ and (f) $Cr_{20}Co_{17.5}Ni_{50}Al_{12.5}$ alloys.

chosen grains of the alloys aged for 50 h and 200 h at 750 °C are shown in Fig. 7. The mean equivalent radius of the precipitates, along with the standard deviation of the measurements, is displayed in the insets of each image. The particles are homogeneously distributed throughout the matrix in all alloys. Since the chemical etching attacks the FCC matrix and the etching depth is both unknown and potentially uneven across the sample, an accurate quantification of the volume fraction of precipitates is not possible.

In both Ti-containing alloys, the particles present a spherical morphology, while in the Ti-free alloy the precipitates show a more irregular morphology. As indicated by the red dashed ellipse, in this latter alloy spherical particles coalesce and give origin to the irregularly shaped precipitates. Usually, the morphology of $L1_2$ precipitates is influenced by the strain energy associated with these precipitates. Consequently, their shape is primarily determined by two key factors: the lattice misfit δ (as defined in Eq. (11) and the size of the precipitates. When the misfit is exceptionally low, precipitates tend to maintain a more spherical shape, even after extended aging treatments. However, as the misfit increases, the morphology of the precipitates may undergo changes during the aging process, leading to the formation of cuboidal shapes or more intricate, complex morphologies.

Representative EDS data of randomly chosen regions, composed of matrix and precipitates, are shown in the table inset in the images in the right column of Fig. 7. The standard deviation of the measurements indicates a very homogeneous chemical composition along the samples. The results also show that the alloys present a chemical composition close to the target ones.

The synchrotron diffraction pattern of the samples in the aged condition are shown in Fig. 8a–b. The $L1_2$ ordered phase has a primitive cubic lattice (space group $Pm\bar{3}m$) and, therefore, it is expected that this

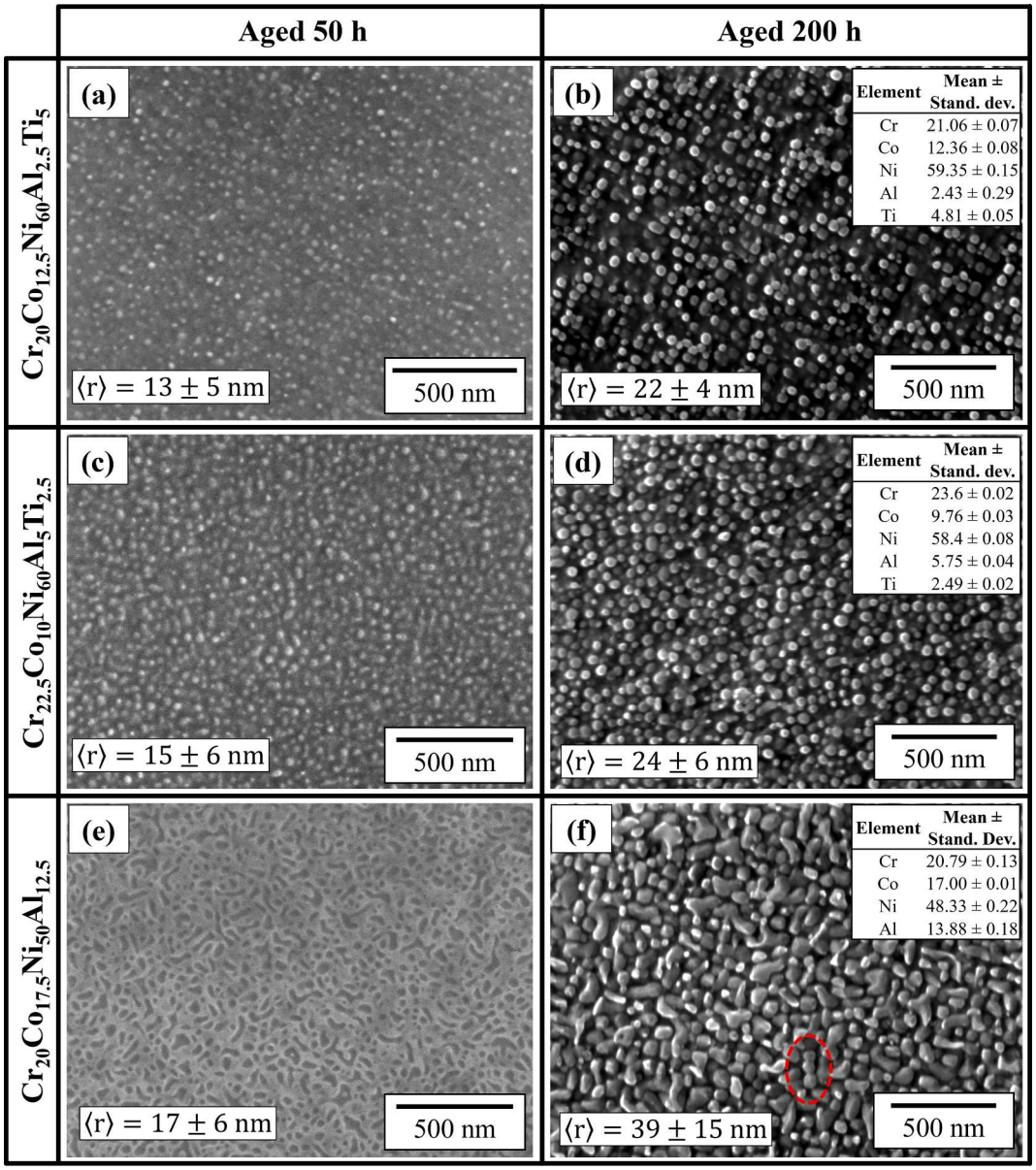

Fig. 7. SEM images acquired using Everhart-Thornley detector of the produced alloys after aging at 750 °C for 50 and 200 h. The left column shows images of (a) $Cr_{20}Co_{12.5}Ni_{60}Al_{2.5}Ti_5$, (c) $Cr_{22.5}Co_{10}Ni_{60}Al_5Ti_{2.5}$, and (e) $Cr_{20}Co_{17.5}Ni_{50}Al_{12.5}$ alloys after aging for 50 h. The right column shows images of (b) $Cr_{20}Co_{12.5}Ni_{60}Al_{2.5}Ti_5$, (d) $Cr_{22.5}Co_{10}Ni_{60}Al_5Ti_{2.5}$, and (f) $Cr_{20}Co_{17.5}Ni_{50}Al_{12.5}$ alloys after aging for 200 h. Before SEM analysis, samples were chemically etched with glyceregia etchant. The inset at the bottom of each image indicates the mean precipitate radius and standard deviation of measurements.

phase present all reflections of such a lattice. Its most intense reflections, also known as fundamental reflections, are those concerning the same planes of the disordered FCC solid solution (space group $Fm\bar{3}m$). On the other hand, the extra reflections of the $L1_2$ phase, termed as superlattice reflections, tends to be very weak due to their low structure factor. This is demonstrated in the simulated diffraction patterns presented in Fig. 8c).

In Ni-superalloys the FCC and $L1_2$ phases typically present similar lattice parameters, with a lattice misfit, given by Eq. (11), generally less than ± 1 % [38]. Consequently, the 2θ position of the FCC reflections and the fundamental reflections of the $L1_2$ phase overlap in the XRD pattern. Since the superlattice reflection tends to be very weak, they are hardly detectable using ordinary XRD equipment. However, with the intense radiation available at synchrotron facilities, these reflections tend to become discernible. At the P07 beamline of the synchrotron radiation facility PETRA III, second harmonics are generated. These harmonics double the photon energy and halve the wavelength of the fundamental radiation. In other words, the synchrotron XRD pattern shows reflection as if the sample interacted with a radiation of wavelengths $\lambda_1 = 0.14235$ Å (first harmonics) and $\lambda_2 = 0.071175$ Å (second harmonics). As a result, for a microstructure consisting of both FCC and $L1_2$ phases, the superlattice reflections of the $L1_2$ phase overlap with the second harmonics of the FCC phase, as indicated in the simulated diffraction pattern presented in Fig. 8c).

$$\delta = 2\frac{a_{L1_2} - a_{FCC}}{a_{FCC} + a_{L1_2}} \tag{11}$$

The hardness as a function of the aging time of $Cr_{20}Co_{12.5}Ni_{60}Al_{2.5}Ti_5$, $Cr_{22.5}Co_{10}Ni_{60}Al_5Ti_{2.5}$, and $Cr_{20}Co_{17.5}Ni_{50}Al_{12.5}$ alloys is shown in Fig. 9. The error bars represent the standard deviation of measurements. In the solution-treated condition, these alloys present hardness values of 313, 270 and 263 HV 0.5, respectively. The CrCoNi alloy is considered one of the strongest single-phase FCC material, with a hardness in the annealed condition for the same grain size (d ~ 120 μm)

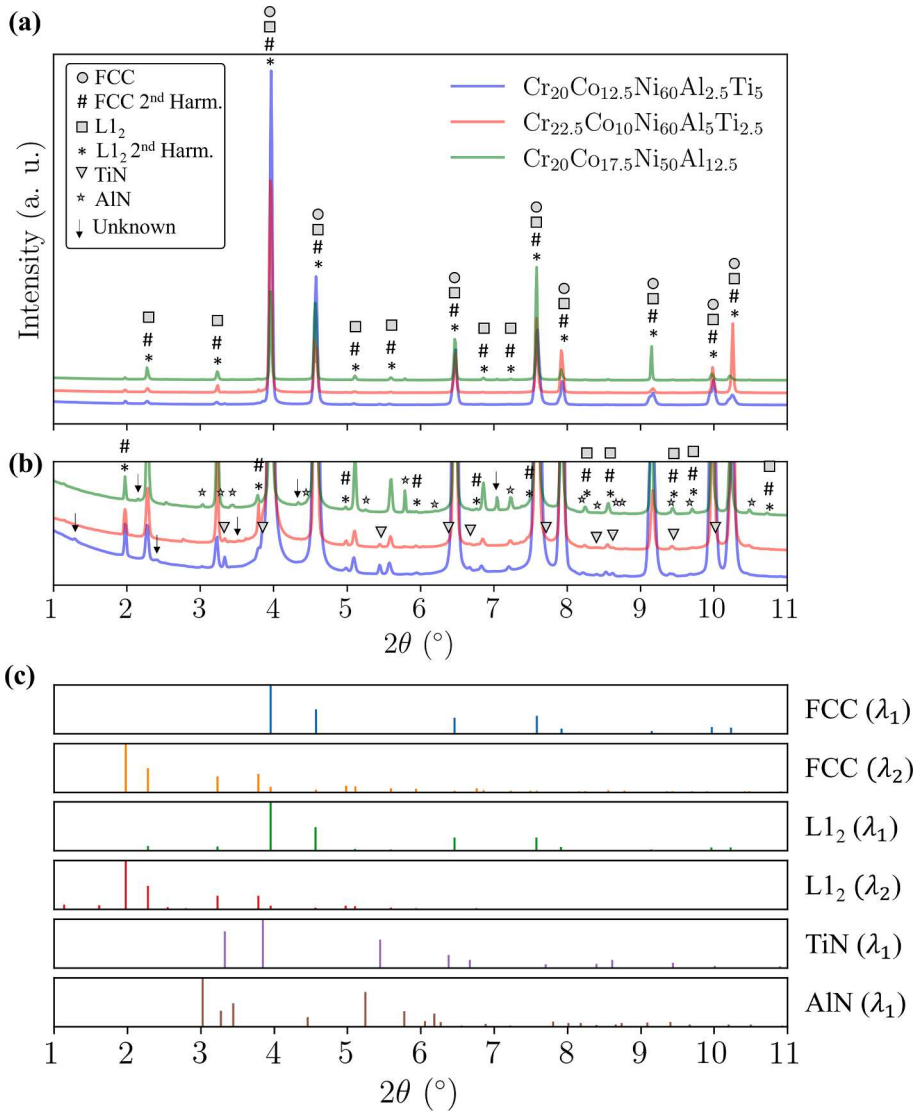

Fig. 8. A) Full synchrotron-XRD patterns of $Cr_{20}Co_{12.5}Ni_{60}Al_{2.5}Ti_5$, $Cr_{22.5}Co_{10}Ni_{60}Al_5Ti_{2.5}$, and $Cr_{20}Co_{17.5}Ni_{50}Al_{12.5}$ alloys in the aged condition; b) enlarged view of the low-intensity range of the patterns shown in (a); and c) simulated diffraction peaks for the FCC, $L1_2$, TiN, and AlN phases with intensities normalized by the most intense peak. λ_1 and λ_2 indicates that the patterns were simulated using a wavelength of 0.14235 and 0.07117 Å, respectively.

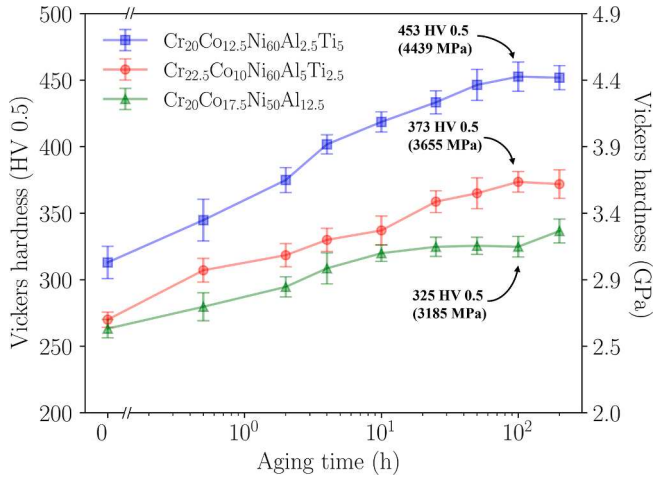

Fig. 9. Hardness as a function of aging time at 750 °C of $Cr_{20}Co_{12.5}Ni_{60}Al_{2.5}Ti_5$, $Cr_{22.5}Co_{10}Ni_{60}Al_5Ti_{2.5}$, and $Cr_{20}Co_{17.5}Ni_{50}Al_{12.5}$ alloys.

of approximately 150 HV [64]. Therefore, the measured values indicates that even in solution treated condition the small precipitates observed in the TEM images has a significant contribution to the material's hardness.

An increase in the hardness value in both Ti-containing alloys is observed until ~ 100 h of aging, and the peak aging condition is achieved in the time interval between 100 and 200 h of heat treatment. On the other hand, the Ti-free alloy reaches the peak aging condition earlier, at about 20 h of treatment, and the hardness remains constant until 200 h of aging. Most likely due to a higher coarsening rate and because of coalescence effect, the Ti-free alloys achieve the critical radius earlier than the Ti-containing alloys.

Tensile engineering stress–strain curves of the selected alloys tested at room temperature, 650, 750, and 850 °C are shown in the Fig. 10a–d, and the yield strength of the alloys as a function of the test temperature is shown in Fig. 11. In all cases, even ignoring the grain boundary hardening mechanism, the proposed model overpredicts the yield strength value. As discussed previously, the peak aged strength contribution equation might fail to quantitatively predict the maximum precipitation hardening contribution but can be used to guide the alloy design.

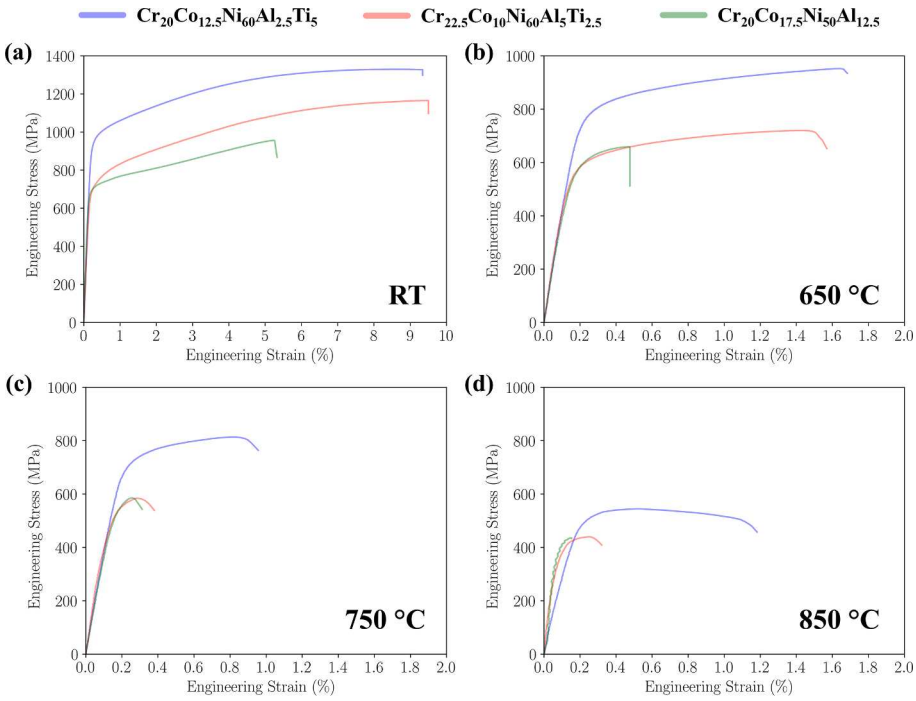

Fig. 10. Tensile engineering stress–strain curves of $Cr_{20}Co_{12.5}Ni_{60}Al_{2.5}Ti_5$, $Cr_{22.5}Co_{10}Ni_{60}Al_5Ti_{2.5}$, and $Cr_{20}Co_{17.5}Ni_{50}Al_{12.5}$ alloys tested at different temperatures: (a) room temperature, (b) 650, (c) 750, and (d) 850 °C.

Despite not showing a quantitative agreement, the experimental trend is successfully captured by the proposed methodology. The $Cr_{20}Co_{12.5}Ni_{60}Al_{2.5}Ti_5$ alloy is in fact the alloy with highest yield stress; even with a volume fraction close to that of $Cr_{22.5}Co_{10}Ni_{60}Al_5Ti_{2.5}$, its strength is 35 % higher. This demonstrates that not only the volume fraction but also the antiphase boundary energy estimation should be taken into consideration during the design of alloys with optimized yield stress, which is well captured by the modeling. Furthermore, even with quite different volume fractions of precipitates, the yield strength of the two latter alloys were close, which is also well captured by the proposed methodology. Therefore, the proposed method provides a promising path for the faster identification and development of new alloys with optimized mechanical properties. Moreover, other variables such as density and alloy's cost can be easily calculated and added to the proposed model, aiding in the choice of the best alloy for a given application.

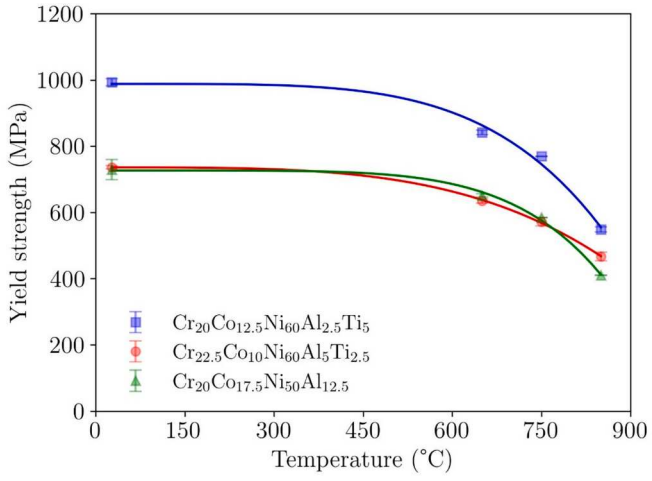

Fig. 11. Yield strength as function of tensile test temperature for $Cr_{20}Co_{12.5}Ni_{60}Al_{2.5}Ti_5$, $Cr_{22.5}Co_{10}Ni_{60}Al_5Ti_{2.5}$, and $Cr_{20}Co_{17.5}Ni_{50}Al_{12.5}$ alloys. The error bars indicate the standard deviation of the measurements.

Fig. 12 illustrates the positioning of the designed alloys in relation to traditional superalloys, considering their yield stress and volume fraction of precipitates. A careful analysis of the composition of the alloy that beats the designed alloys in terms of yield stress reveals that most of them present molybdenum and/or niobium in their composition. As shown by Chen et al. [57], small addition of these elements to the Ni_3Al structure has one of the greatest potential to increase the APB per unit atom. Besides that, Nb additions tends to stabilize the $D0_{22}$ phase, which also contributes significantly to the increase of yield stress, as in the case of Inconel 718, a benchmark wrought alloy widely employed in high-temperature applications.

The evaluation of APB energy in multicomponent alloys is complex. A deep understanding of χ_{APB} is crucial for designing alloys with optimized properties, and this has been the focus of considerable attention in recent literature [57,65–67]. As discussed previously, there is still a need of development of APB models for multicomponent systems. Besides that, it is important to note that optimizing the APB energy alone is not sufficient for effective alloy design. As previously demonstrated, certain elements can have a beneficial effect on APB energy, but excessive addition may result in the formation of other phases that can be detrimental to mechanical properties or may lack the presence of FCC single phase field at high temperatures. Therefore, developing models that integrate both antiphase boundary energy and phase equilibrium predictions is a promising path for advancing alloy development. In addition, beyond yield stress modeling, other estimations like alloy density and creep resistance, alongside considering the alloy cost, can complement the existing modeling strategy. This holistic approach enhances the capability to develop compositions more tailored and optimized for specific applications.

As shown previously in Fig. 10, at room temperature, the alloys presented high yield strength values and moderate ductility under tension. However, at higher temperatures, the alloys displayed a poor ductility. Fracture surface images of the tested specimens are shown Fig. 13. At room temperature, the specimens exhibit a mixed

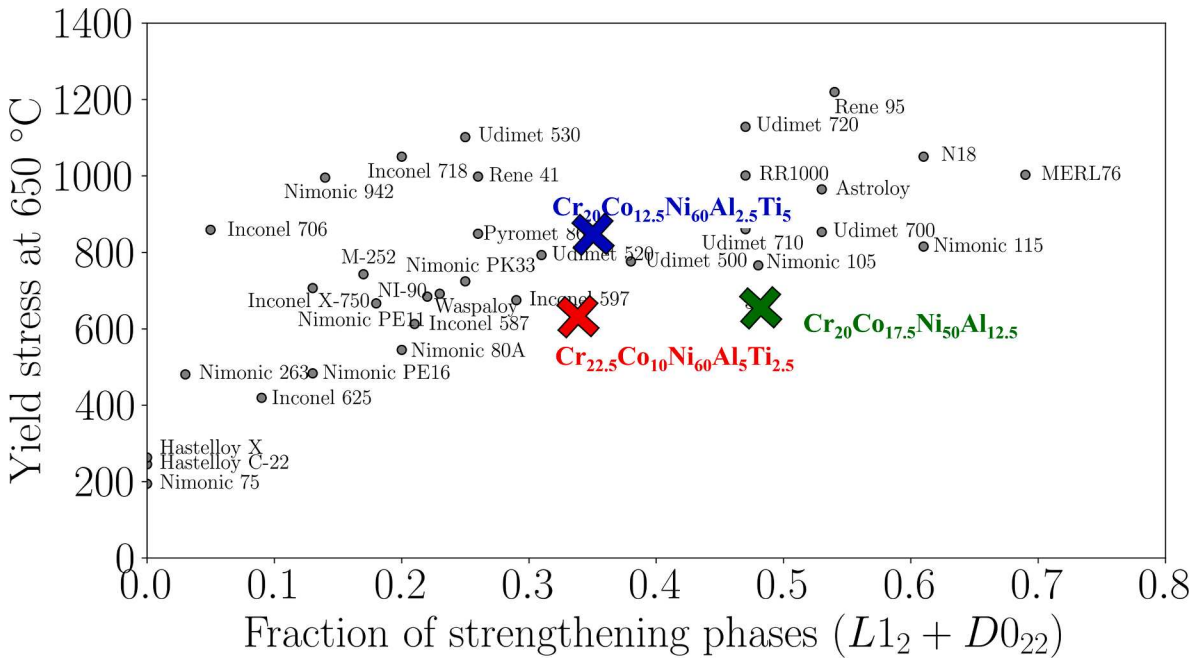

Fig. 12. Comparison of the selected alloys to commercially available wrought superalloys in terms of yield stress at 650 °C and the overall fraction of strengthening phases ($L1_2$ + $D0_{22}$). Data of commercial superalloys were extracted from reference [20].

intergranular-dimpled fracture mode, while at elevated temperatures, a distinctly brittle intergranular fracture is observed in the tested specimens.

Fig. 14 shows SEM images of the grain boundary microstructure of the designed alloys after aging treatment at 750 °C for 200 h. At this condition, discontinuous precipitation colonies can be observed along the grain boundaries in all alloys.

Discontinuous precipitation (DP), also known as cellular precipitation, is defined as a solid-state precipitation reaction characterized by grain boundary migration with the growing cell tips [68,69]. The DP cells may grow in only one direction or in opposite directions from the original grain-boundary position. This reaction has been observed for a long time in a wide range of alloys, ranging from simple binaries, for example Pb-Sn [70], to more complex systems such as those of ferritic steels [71], austenitic steels [72], and superalloys [73,74]. Recently, such undesired precipitation behavior has been reported in several HEAs [75–80].

Although the understanding of discontinuous precipitation reaction is desirable, the precise conditions, during which DP occurs or is preferred over continuous precipitation (CP), are still a matter of controversy in the literature. The reaction initiation may change in the same system depending on aging temperatures. Furthermore, it may differ from one alloy to another, even in a similar class of alloys, and it may be more complex in multicomponent systems. For example, Nystrom et al. [81] investigated a refractory nickel superalloy ($Ni_{61.1}Cr_{5.4}Co_{13.2}Al_{13.8}W_2Hf_{0.1}Re_{2.1}Ta_{2.4}$, in at.%) and noticed the following reaction on grain boundary FCC+$L1_2$ → FCC_{cell} + $L1_{2cell}$ + TCP, where TPC is a rhenium-rich Topological Close Packed (TCP) phase, identified as the P-phase by the authors. A similar behavior was observed for a variation of commercial nickel superalloys CMSX-4 with high-Re content [82]. On the other hand, Yang and coworkers [83] studied the $Ni_{29.9}Cr_{15}Co_{30}Fe_{13}Al_6Ti_6B_{0.1}$ (at. %) alloy. They observed a two-step discontinuous reaction along the grain boundaries. First, the coherent, discrete $L1_2$ precipitates embedded in an FCC matrix transformed to a lamellar FCC plus metastable $L1_2$ phase along the grain boundaries. With the progress of aging, the lamellae FCC plus metastable $L1_2$ transformed into a lamellar (FCC+$L1_2$) + blocky Heusler ($L2_1$) phase.

Despite the potential decrease in ductility caused by the DP, the grain boundary microstructure is expected to remain relatively stable throughout the tensile test. All elements in the alloys are of the substitutional type, and their diffusion is likely to be limited within the short timeframe of the mechanical test, which typically lasts only a few minutes. Therefore, an increase in ductility was expected as the test temperature increased, which is in contrast with experimental observations. Conversely, different works [84–86] demonstrate that superalloys may show a ductile to brittle transition behavior at temperatures in the range of approximately 600–900 °C. This behavior is related to the diffusion of oxygen from the atmosphere through the grain boundaries. The internal oxidation may form complex oxide phases that weaken the grain boundary cohesion, facilitating crack initiation and propagation under mechanical stress. Since discontinuous precipitation is a controversial topic in the literature, and the study of the embrittlement requires an in-depth characterization analysis, these studies are suggested as future works.

5. Conclusions

In this work, a novel strategy for designing multicomponent alloys consisting of an FCC matrix, $L1_2$ precipitates, and optimized yield stress was proposed. The of analyses of both thermodynamic data and mathematical modeling of yield stress revealed that the solid solution contribution only slightly changes across different alloys in the Cr-Co-Ni-Al-Ti system. The yield stress is dominated by the precipitation hardening contribution. The data analysis also allowed to conclude that, although increasing titanium concentration in the alloys significantly enhances the antiphase boundary energy, a concentration greater or equal to 7.5 % results in the absence of a single-phase FCC field at high temperatures, limiting the alloy's ability to undergo precipitation hardening.

Three alloys were selected and produced to test the effectiveness of the proposed strategy for alloy design. The experimental results showed that the intended microstructure was achieved, with the alloys consisting of an FCC matrix and dispersed $L1_2$ precipitates, demonstrating an accurate description of the CALPHAD database for the Cr-Co-Ni-Al-Ti system. More importantly, tensile tests showed that the proposed strategy successfully captures the trends in yield strength. When

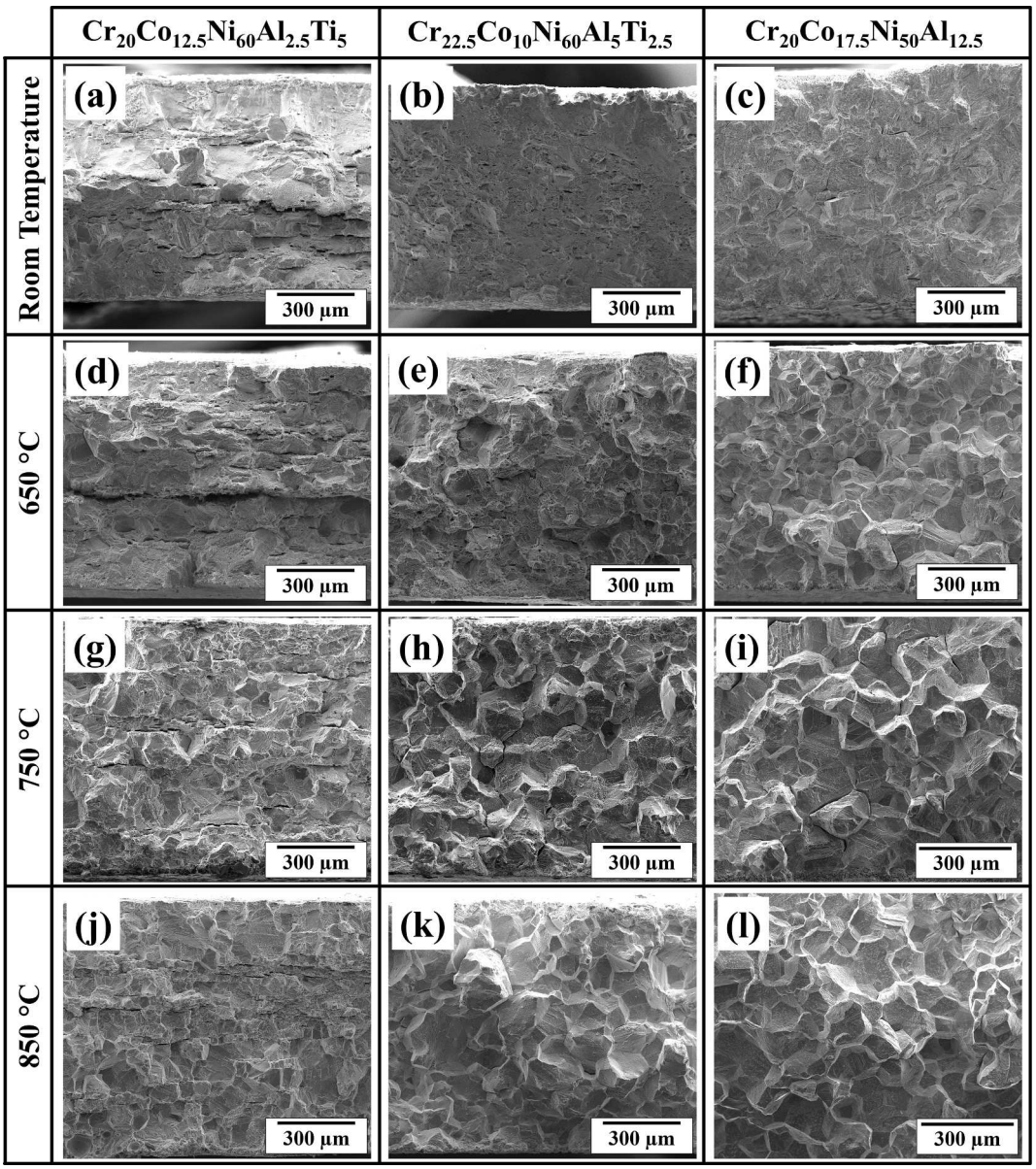

Fig. 13. SEM images acquired using Everhart-Thornley detector of the fracture surface of tensile test specimens of $Cr_{20}Co_{12.5}Ni_{60}Al_{2.5}Ti_{5,}$ $Cr_{22.5}Co_{10}Ni_{60}Al_5Ti_{2.5,}$ and $Cr_{20}Co_{17.5}Ni_{50}Al_{12.5}$ alloys tested at different temperatures. All images were acquired at the same magnification. Post-morten fracture surface images of specimens of the produced alloys tested at different temperatures. The images were obtained by SEM using the ET detector. The left column corresponds to images of $Cr_{20}Co_{12.5}Ni_{60}Al_{2.5}Ti_5$ alloy tested at (a) room temperature, (d) 650, (g) 750, and (j) 850 °C. The centered column corresponds to images of $Cr_{22.5}Co_{10}Ni_{60}Al_5Ti_{2.5}$ alloy tested at (b) room temperature, (e) 650, (h) 750, and (k) 850 °C. The right column correspond to images of $Cr_{20}Co_{17.5}Ni_{50}Al_{12.5}$ alloy tested at (c) room temperature, (f) 650, (i) 750 (l) 850 °C.

comparing the composition of the most promising alloy with those of commercially available wrought superalloys with superior strength, it was found that incorporating Mo and Nb in the studied system is highly promising, since these elements show one of the greatest potentials to increase the APB per unit atom.

Overall, this work showed that the integration of high-throughput thermodynamic calculation and property modeling is an effective strategy to explore the landscape of a multicomponent, multiphase system. Furthermore, the method is highly versatile and can be adapted to incorporate the prediction of more than one property during the design stage. This approach has the potential to accelerate the discovery and development of novel HEAs with promising properties and the capability to develop compositions more tailored and optimized for specific applications.

CRediT authorship contribution statement

Diego de Araujo Santana: Writing – original draft, Visualization, Validation, Methodology, Investigation, Formal analysis, Data curation, Conceptualization. **Benjamin Ellyson:** Investigation, Formal analysis. **Amy Clarke:** Writing – review & editing, Supervision, Resources, Conceptualization. **Kester Clarke:** Writing – review & editing, Supervision, Resources, Funding acquisition. **Norbert Schell:** Investigation, Data curation. **Michael Kaufman:** Writing – review & editing, Supervision, Resources, Project administration, Investigation, Conceptualization. **Claudio Shyinti Kiminami:** Writing – review & editing, Supervision, Resources, Project administration, Methodology, Funding acquisition, Conceptualization. **Francisco Gil Coury:** Writing – review & editing, Supervision, Resources, Project administration, Methodology, Investigation, Funding acquisition, Conceptualization.

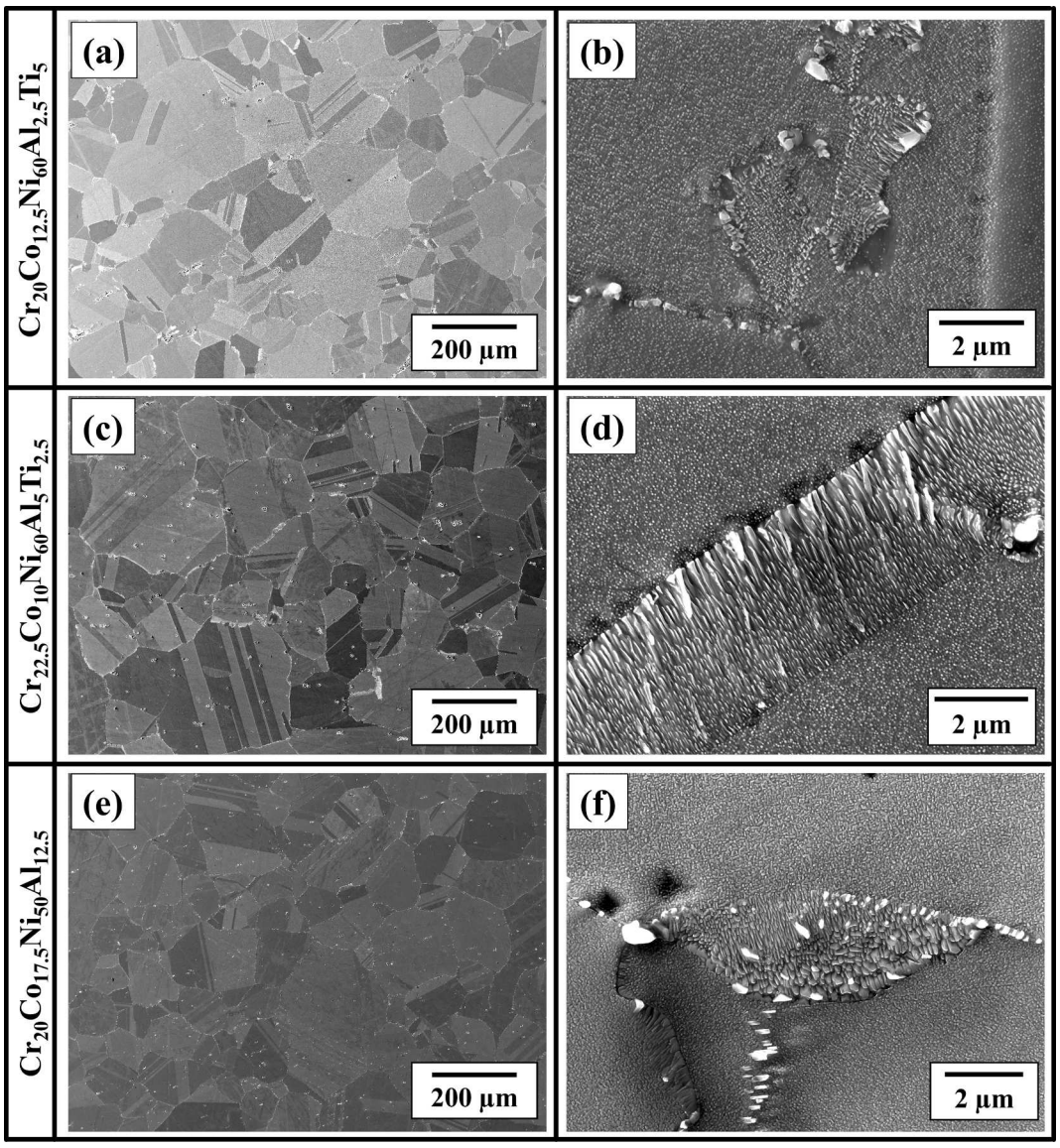

Fig. 14. SEM images of grain boundaries microstructure of $Cr_{20}Co_{12.5}Ni_{60}Al_{2.5}Ti_5$, $Cr_{22.5}Co_{10}Ni_{60}Al_5Ti_{2.5}$, and $Cr_{20}Co_{17.5}Ni_{50}Al_{12.5}$ alloys after aging treatment at 750 °C for 200 h. All images were acquired using Everhart-Thornley detector. SEM images, acquired using Everhart-Thornley detector, of grain boundaries microstructure of produced alloys after aging treatment at 750 °C for 200 h at different magnification. Images in the first row, (a) and (b), correspond to microstructure of $Cr_{20}Co_{12.5}Ni_{60}Al_{2.5}Ti_5$, images in the second row corresponds to microstructure of $Cr_{22.5}Co_{10}Ni_{60}Al_5Ti_{2.5}$, and images in the third row correspond to microstructure of $Cr_{20}Co_{17.5}Ni_{50}Al_{12.5}$ alloy.

Declaration of competing interest

The authors declare that they have no known competing financial interests or personal relationships that could have appeared to influence the work reported in this paper.

Data availability

Data will be made available on request.

Acknowledgements

This work was financed in part by the Coordenação de Aperfeiçoamento de Pessoal de Nível Superior - Brasil (CAPES) - Finance Code 001, Conselho Nacional de Desenvolvimento Científico e Tecnológico (CNPq) and by São Paulo Research Foundation (FAPESP) [grant #2018/26390-3, São Paulo Research Foundation (FAPESP), grant#2021/04302-8, São Paulo Research Foundation (FAPESP)]. The authors thank the Laboratory of Structural Characterization (LCE/DEMa/UFSCar) for the general facilities. Also, the authors would like to thank Drs. Fan Zhang and Chuan Zhang as well as the COMPUTHERM LCC™ company for providing a Pandat™ license and the necessary thermodynamic databases. We acknowledge DESY (Hamburg, Germany), a member of the Helmholtz Association HGF, for the provision of experimental facilities. Parts of this research were carried out at P07B and we would like to thank Dr. Norbert Schell for assistance in using the beamline. Beamtime was allocated for proposal I-20220798. The research was sponsored by the Army Research Office and was accomplished under Grant Number W911NF-23-1-0310. The views and conclusions contained in this document are those of the authors and should not be interpreted as representing the official policies, either expressed or implied, of the Army Research Office or the U.S. Government. The U.S. Government is authorized to reproduce and distribute reprints for Government purposes notwithstanding any copyright notation herein.

References

[1] J.-W. Yeh, S.-K. Chen, S.-J. Lin, J.-Y. Gan, T.-S. Chin, T.-T. Shun, C.-H. Tsau, S.-Y. Chang, Nanostructured High-Entropy Alloys with Multiple Principal Elements: Novel Alloy Design Concepts and Outcomes, Adv. Eng. Mater. 6 (2004) 299–303, https://doi.org/10.1002/adem.200300567.

[2] T.K. Chen, T.T. Shun, J.W. Yeh, M.S. Wong, Nanostructured nitride films of multi-element high-entropy alloys by reactive DC sputtering, Surf. Coat. Technol. 188–189 (2004) 193–200, https://doi.org/10.1016/j.surfcoat.2004.08.023.

[3] P.-K. Huang, J.-W. Yeh, T.-T. Shun, S.-K. Chen, Multi-Principal-Element Alloys with Improved Oxidation and Wear Resistance for Thermal Spray Coating, Adv. Eng. Mater. 6 (2004) 74–78, https://doi.org/10.1002/adem.200300507.

[4] C.K.H. Borg, C. Frey, J. Moh, T.M. Pollock, S. Gorsse, D.B. Miracle, O.N. Senkov, B. Meredig, J.E. Saal, Expanded dataset of mechanical properties and observed phases of multi-principal element alloys, Sci. Data 7 (2020) 430, https://doi.org/10.1038/s41597-020-00768-9.

[5] F. Otto, Y. Yang, H. Bei, E.P. George, Relative effects of enthalpy and entropy on the phase stability of equiatomic high-entropy alloys, Acta Mater. 61 (2013) 2628–2638, https://doi.org/10.1016/j.actamat.2013.01.042.

[6] F.G. Coury, P. Wilson, K.D. Clarke, M.J. Kaufman, A.J. Clarke, High-throughput solid solution strengthening characterization in high entropy alloys, Acta Mater. 167 (2019) 1–11, https://doi.org/10.1016/j.actamat.2019.01.029.

[7] F.G. Coury, K.D. Clarke, C.S. Kiminami, M.J. Kaufman, A.J. Clarke, High Throughput Discovery and Design of Strong Multicomponent Metallic Solid Solutions, Sci. Rep. 8 (2018) 8600, https://doi.org/10.1038/s41598-018-26830-6.

[8] Z. Wu, H. Bei, G.M. Pharr, E.P. George, Temperature dependence of the mechanical properties of equiatomic solid solution alloys with face-centered cubic crystal structures, Acta Mater. 81 (2014) 428–441, https://doi.org/10.1016/j.actamat.2014.08.026.

[9] B. Gludovatz, A. Hohenwarter, K.V.S. Thurston, H. Bei, Z. Wu, E.P. George, R. O. Ritchie, Exceptional damage-tolerance of a medium-entropy alloy CrCoNi at cryogenic temperatures, Nat. Commun. 7 (2016) 10602, https://doi.org/10.1038/ncomms10602.

[10] D. Liu, Q. Yu, S. Kabra, M. Jiang, P. Forna-Kreutzer, R. Zhang, M. Payne, F. Walsh, B. Gludovatz, M. Asta, A.M. Minor, E.P. George, R.O. Ritchie, Exceptional fracture toughness of CrCoNi-based medium- and high-entropy alloys at 20 kelvin, Science 378 (2022) 978–983, https://doi.org/10.1126/science.abp8070.

[11] D.B. Miracle, O.N. Senkov, A critical review of high entropy alloys and related concepts, Acta Mater. 122 (2017) 448–511, https://doi.org/10.1016/j.actamat.2016.08.081.

[12] Y.-T. Chen, Y.-J. Chang, H. Murakami, S. Gorsse, A.-C. Yeh, Designing high entropy superalloys for elevated temperature application, Scr. Mater. 187 (2020) 177–182, https://doi.org/10.1016/j.scriptamat.2020.06.002.

[13] B. Gwalani, D. Choudhuri, V. Soni, Y. Ren, M. Styles, J.Y. Hwang, S.J. Nam, H. Ryu, S.H. Hong, R. Banerjee, Cu assisted stabilization and nucleation of L12 precipitates in Al0.3CuFeCrNi2 fcc-based high entropy alloy, Acta Mater. 129 (2017) 170–182, https://doi.org/10.1016/j.actamat.2017.02.053.

[14] Y.-T. Chen, Y.-J. Chang, H. Murakami, T. Sasaki, K. Hono, C.-W. Li, K. Kakehi, J.-W. Yeh, A.-C. Yeh, Hierarchical microstructure strengthening in a single crystal high entropy superalloy, Sci. Rep. 10 (2020) 12163, https://doi.org/10.1038/s41598-020-69257-8.

[15] D.B. Miracle, M.-H. Tsai, O.N. Senkov, V. Soni, R. Banerjee, Refractory high entropy superalloys (RSAs), Scr. Mater. 187 (2020) 445–452, https://doi.org/10.1016/j.scriptamat.2020.06.048.

[16] J.-P. Couzinié, M. Heczko, V. Mazánová, O.N. Senkov, M. Ghazisaeidi, R. Banerjee, M.J. Mills, High-temperature deformation mechanisms in a BCC+B2 refractory complex concentrated alloy, Acta Mater. 233 (2022) 117995, https://doi.org/10.1016/j.actamat.2022.117995.

[17] P. Kumar, S.J. Kim, Q. Yu, J. Ell, M. Zhang, Y. Yang, J.Y. Kim, H.-K. Park, A. M. Minor, E.S. Park, R.O. Ritchie, Compressive vs. tensile yield and fracture toughness behavior of a body-centered cubic refractory high-entropy superalloy Al0.5Nb1.25Ta1.25TiZr at temperatures from ambient to 1200°C, Acta Mater. 245 (2023) 118620, https://doi.org/10.1016/j.actamat.2022.118620.

[18] S. Gorsse, J.-P. Couzinié, D.B. Miracle, From high-entropy alloys to complex concentrated alloys, Comptes Rendus Phys. 19 (2018) 721–736, https://doi.org/10.1016/j.crhy.2018.09.004.

[19] W. Cao, S.-L. Chen, F. Zhang, K. Wu, Y. Yang, Y.A. Chang, R. Schmid-Fetzer, W. A. Oates, PANDAT software with PanEngine, PanOptimizer and PanPrecipitation for multi-component phase diagram calculation and materials property simulation, Calphad 33 (2009) 328–342, https://doi.org/10.1016/j.calphad.2008.08.004.

[20] R.C. Reed, The Superalloys: Fundamentals and Applications, 1st ed., Cambridge University Press, 2006. https://doi.org/10.1017/CBO9780511541285.

[21] M.J. Donachie, S.J. Donachie, Superalloys: a technical guide, 2nd ed., ASM International, Materials Park, OH, 2002.

[22] A.S. Argon, Strengthening mechanisms in crystal plasticity, Oxford University Press, Oxford; New York, 2008.

[23] H. Pottebohm, G. Neite, E. Nembach, Elastic properties (the stiffness constants, the shear modulus and the dislocation line energy and tension) of Ni-Al solid solutions and of the Nimonic alloy PE16, Mater. Sci. Eng. 60 (1983) 189–194, https://doi.org/10.1016/0025-5416(83)90001-0.

[24] N. Parveen, G.V.S. Murthy, Determination of elastic modulus in a nickel alloy from ultrasonic measurements, Bull. Mater. Sci. 34 (2011) 323–326, https://doi.org/10.1007/s12034-011-0070-z.

[25] B. Reppich, P. Schepp, G. Wehner, Some new aspects concerning particle hardening mechanisms in γ' precipitating nickel-base alloys—II. Experiments, Acta Metall. 30 (1982) 95–104, https://doi.org/10.1016/0001-6160(82)90049-9.

[26] S. Yoshitake, V. Narayan, H. Harada, H.K.D.H. Bhadeshia, D.J.C. Mackay, Estimation of the .GAMMA. and .GAMMA.' Lattice Parameters in Nickel-base Superalloys Using Neural Network Analysis., ISIJ Int. 38 (1998) 495–502. https://doi.org/10.2355/isijinternational.38.495.

[27] F. Wallow, E. Nembach, Synergisms of grain boundary and γ′-particle strengthening in nickel-base superalloys, Scr. Mater. 34 (1996) 499–505, https://doi.org/10.1016/S0956-716X(95)00548-A.

[28] L. Connor, The Development of a dual microstructure heat treated superalloy for turbine disc applications, University of Cambridge, PhD, 2009.

[29] H.A. Roth, C.L. Davis, R.C. Thomson, Modeling solid solution strengthening in nickel alloys, Metall. Mater. Trans. A 28 (1997) 1329–1335, https://doi.org/10.1007/s11661-997-0268-2.

[30] E.I. Galindo-Nava, L.D. Connor, C.M.F. Rae, On the prediction of the yield stress of unimodal and multimodal γ′ Nickel-base superalloys, Acta Mater. 98 (2015) 377–390, https://doi.org/10.1016/j.actamat.2015.07.048.

[31] C. Varvenne, A. Luque, W.A. Curtin, Theory of strengthening in fcc high entropy alloys, Acta Mater. 118 (2016) 164–176, https://doi.org/10.1016/j.actamat.2016.07.040.

[32] C. Varvenne, G.P.M. Leyson, M. Ghazisaeidi, W.A. Curtin, Solute strengthening in random alloys, Acta Mater. 124 (2017) 660–683, https://doi.org/10.1016/j.actamat.2016.09.046.

[33] B. Yin, W.A. Curtin, First-principles-based prediction of yield strength in the RhIrPdPtNiCu high-entropy alloy, Npj Comput. Mater. 5 (2019) 14, https://doi.org/10.1038/s41524-019-0151-x.

[34] C. Varvenne, W.A. Curtin, Strengthening of high entropy alloys by dilute solute additions: CoCrFeNiAl and CoCrFeNiMnAl alloys, Scr. Mater. 138 (2017) 92–95, https://doi.org/10.1016/j.scriptamat.2017.05.035.

[35] D. De Araujo Santana, C.S. Kiminami, F.G. Coury, Mechanical properties and yield strength modeling of a medium entropy alloy containing L12 precipitates, J. Alloys Compd. 898 (2022) 162923, https://doi.org/10.1016/j.jallcom.2021.162923.

[36] A.J. Ardell, Precipitation hardening, Metall. Trans. A 16 (1985) 2131–2165, https://doi.org/10.1007/BF02670416.

[37] E. Nembach, K. Suzuki, M. Ichihara, S. Takeuchi, In situ deformation of the γ' hardened superalloy Nimonic PE16 in high-voltage electron microscopes, Philos. Mag. A 51 (1985) 607–618, https://doi.org/10.1080/01418618508237581.

[38] E. Nembach, G. Neite, Precipitation hardening of superalloys by ordered γ′-particles, Prog. Mater. Sci. 29 (1985) 177–319, https://doi.org/10.1016/0079-6425(85)90001-5.

[39] A.J. Ardell, Ch 12: Intermetallics as Precipitates and Dispersoids in High-Strength Alloys, Intermet. Compd., John Wiley & Sons, 1994, pp. 257–286.

[40] T. Kruml, E. Conforto, B. Lo Piccolo, D. Caillard, J.L. Martin, From dislocation cores to strength and work-hardening: a study of binary Ni3Al, Acta Mater. 50 (2002) 5091–5101, https://doi.org/10.1016/S1359-6454(02)00364-6.

[41] H.P. Karnthaler, E.T. Mühlbacher, C. Rentenberger, The influence of the fault energies on the anomalous mechanical behaviour of Ni3Al alloys, Acta Mater. 44 (1996) 547–560, https://doi.org/10.1016/1359-6454(95)00191-3.

[42] D.M. Dimiduk, A.W. Thompson, J.C. Williams, The compositional dependence of antiphase-boundary energies and the mechanism of anomalous flow in Ni $_3$ Al alloys, Philos. Mag. A 67 (1993) 675–698, https://doi.org/10.1080/01418619308207184.

[43] A.J. Ardell, V. Munjal, D.J. Chellman, Precipitation hardening of Ni-Al alloys containing large volume fractions of γ′, Metall. Trans. A 7 (1976) 1263–1268, https://doi.org/10.1007/BF02658809.

[44] P.A. Flinn, Theory of Deformation in Superlattices, Trans. Am. Inst. Min. Metall. Eng. 218 (1960) 145–154.

[45] V. Paidar, The structure and energy of antiphase boundaries in Ll2 alloys, Acta Metall. 33 (1985) 1803–1811, https://doi.org/10.1016/0001-6160(85)90004-5.

[46] G. Inden, S. Bruns, H. Ackermann, Antiphase boundary energies in ordered f.c.c. alloys, Philos. Mag. A 53 (1986) 87–100, https://doi.org/10.1080/01418618608242809.

[47] A.G. Khachaturyan, J.W. Morris, The interfacial tension of a sharp antiphase domain boundary, Philos. Mag. A 56 (1987) 517–532, https://doi.org/10.1080/01418618708214403.

[48] A.P. Miodownik, N. Saunders, The calculation of APB energies in L12 compounds using a thermodynamic database, in: Appl. Thermodyn. Synth. Process. Mater., TMS, 1995: pp. 91–104.

[49] N. Saunders, M. Fahrmann, C.J. Small, The Application of Calphad Calculations to Ni-Based Superalloys, in: Superalloys 2000 Ninth Int. Symp., TMS, 2000: pp. 803–811. https://doi.org/10.7449/2000/Superalloys_2000_803_811.

[50] Y.-K. Kim, D. Kim, H.-K. Kim, E.-Y. Yoon, Y. Lee, C.-S. Oh, B.-J. Lee, A numerical model to predict mechanical properties of Ni-base disk superalloys, Int. J. Plast. 110 (2018) 123–144, https://doi.org/10.1016/j.ijplas.2018.06.011.

[51] D.M. Collins, H.J. Stone, A modelling approach to yield strength optimisation in a nickel-base superalloy, Int. J. Plast. 54 (2014) 96–112, https://doi.org/10.1016/j.ijplas.2013.08.009.

[52] D.J. Crudden, A. Mottura, N. Warnken, B. Raeisinia, R.C. Reed, Modelling of the influence of alloy composition on flow stress in high-strength nickel-based superalloys, Acta Mater. 75 (2014) 356–370, https://doi.org/10.1016/j.actamat.2014.04.075.

[53] M. Dodaran, A.H. Ettefagh, S.M. Guo, M.M. Khonsari, W.J. Meng, N. Shamsaei, S. Shao, Effect of alloying elements on the γ' antiphase boundary energy in Ni-base superalloys, Intermetallics 117 (2020) 106670, https://doi.org/10.1016/j.intermet.2019.106670.

[54] K.V. Vamsi, S. Karthikeyan, Modeling APB energies in multicomponent Ni-base superalloys, Intermetallics 132 (2021) 107124, https://doi.org/10.1016/j.intermet.2021.107124.

[55] O.I. Gorbatov, I.L. Lomaev, Y.N. Gornostyrev, A.V. Ruban, D. Furrer, V. Venkatesh, D.L. Novikov, S.F. Burlatsky, Effect of composition on antiphase boundary energy in Ni 3 Al based alloys: *Ab initio* calculations, Phys. Rev. B 93 (2016) 224106, https://doi.org/10.1103/PhysRevB.93.224106.
[56] K. Kumar, R. Sankarasubramanian, U.V. Waghmare, Tuning planar fault energies of Ni3Al with substitutional alloying: First-principles description for guiding rational alloy design, Scr. Mater. 142 (2018) 74–78, https://doi.org/10.1016/j.scriptamat.2017.08.021.
[57] E. Chen, A. Tamm, T. Wang, M.E. Epler, M. Asta, T. Frolov, Modeling antiphase boundary energies of Ni3Al-based alloys using automated density functional theory and machine learning, Npj Comput. Mater. 8 (2022) 80, https://doi.org/10.1038/s41524-022-00755-1.
[58] E04 Committee, Test Method for Microindentation Hardness of Materials, ASTM International, n.d. https://doi.org/10.1520/E0384-17.
[59] D. Baither, C. Rentenberger, H.P. Karnthaler, E. Nembach, Three alternative experimental methods to determine the antiphase-boundary energies of the γ′ precipitates in superalloys, Philos. Mag. A 82 (2002) 1795–1805, https://doi.org/10.1080/01418610208235690.
[60] R.W. Cahn, P.A. Siemers, J.E. Geiger, P. Bardhan, The order-disorder transformation in Ni3Al and Ni3Al-Fe alloys—I. Determination of the Transition Temperatures and Their Relation to Ductility, Acta Metall. 35 (1987) 2737–2751, https://doi.org/10.1016/0001-6160(87)90273-2.
[61] N. Baluc, H.P. Karnthaler, M.J. Mills, TEM observation of the fourfold dissociation of superlattice dislocations and the determination of the fault energies in Ni $_3$ (A1, Ta), Philos. Mag. A 64 (1991) 137–150, https://doi.org/10.1080/01418619108206131.
[62] H. Okamoto, M.E. Schlesinger, E.M. Mueller, eds., Alloy Phase Diagrams, ASM International, 2016. https://doi.org/10.31399/asm.hb.v03.9781627081634.
[63] A. Mitchell, Nitrogen in Superalloys, High Temp. Mater. Process. 24 (2005) 101–110, https://doi.org/10.1515/HTMP.2005.24.2.101.
[64] Y.-C. Huang, C.-H. Su, S.-K. Wu, C. Lin, A Study on the Hall-Petch Relationship and Grain Growth Kinetics in FCC-Structured High/Medium Entropy Alloys, Entropy 21 (2019) 297, https://doi.org/10.3390/e21030297.
[65] K.V. Vamsi, T.M. Pollock, A new proximate structure for the APB (111) in L12 compounds, Scr. Mater. 182 (2020) 38–42, https://doi.org/10.1016/j.scriptamat.2020.02.038.
[66] K.V. Vamsi, S. Karthikeyan, High-throughput estimation of planar fault energies in A3B compounds with L12 structure, Acta Mater. 145 (2018) 532–542, https://doi.org/10.1016/j.actamat.2017.10.029.
[67] A. Breidi, J. Allen, A. Mottura, First-principles modeling of superlattice intrinsic stacking fault energies in Ni3Al based alloys, Acta Mater. 145 (2018) 97–108, https://doi.org/10.1016/j.actamat.2017.11.042.
[68] I. Manna, S.K. Pabi, W. Gust, Discontinuous reactions in solids, Int. Mater. Rev. 46 (2001) 53–91, https://doi.org/10.1179/095066001101528402.
[69] D.B. Williams, E.P. Butler, Grain boundary discontinuous precipitation reactions, Int. Met. Rev. 26 (1981) 153–183, https://doi.org/10.1179/imtr.1981.26.1.153.
[70] K.N. Tu, D. Turnbull, Morphology of cellular precipitation of tin from lead-tin bicrystals, Acta Metall. 15 (1967) 369–376, https://doi.org/10.1016/0001-6160(67)90214-3.
[71] B.C. Zhou, T. Yang, G. Zhou, H. Wang, J.H. Luan, Z.B. Jiao, Mechanisms for suppressing discontinuous precipitation and improving mechanical properties of NiAl-strengthened steels through nanoscale Cu partitioning, Acta Mater. 205 (2021) 116561, https://doi.org/10.1016/j.actamat.2020.116561.
[72] R.D. Knutsen, C.I. Lang, J.A. Basson, Discontinuous cellular precipitation in a Cr–Mn–N steel with niobium and vanadium additions, Acta Mater. 52 (2004) 2407–2417, https://doi.org/10.1016/j.actamat.2004.01.031.
[73] A. Devaraj, L. Kovarik, E. Kautz, B. Arey, S. Jana, C. Lavender, V. Joshi, Grain boundary engineering to control the discontinuous precipitation in multicomponent U10Mo alloy, Acta Mater. 151 (2018) 181–190, https://doi.org/10.1016/j.actamat.2018.03.039.
[74] E.J. Pickering, H. Mathur, A. Bhowmik, O.M.D.M. Messé, J.S. Barnard, M.C. Hardy, R. Krakow, K. Loehnert, H.J. Stone, C.M.F. Rae, Grain-boundary precipitation in Allvac 718Plus, Acta Mater. 60 (2012) 2757–2769, https://doi.org/10.1016/j.actamat.2012.01.042.
[75] Y.L. Zhao, T. Yang, Y. Tong, J. Wang, J.H. Luan, Z.B. Jiao, D. Chen, Y. Yang, A. Hu, C.T. Liu, J.-J. Kai, Heterogeneous precipitation behavior and stacking-fault-mediated deformation in a CoCrNi-based medium-entropy alloy, Acta Mater. 138 (2017) 72–82, https://doi.org/10.1016/j.actamat.2017.07.029.
[76] L. Fan, T. Yang, J.H. Luan, Z.B. Jiao, Control of discontinuous and continuous precipitation of γ'-strengthened high-entropy alloys through nanoscale Nb segregation and partitioning, J. Alloys Compd. 832 (2020) 154903, https://doi.org/10.1016/j.jallcom.2020.154903.
[77] N. An, Y. Sun, Y. Wu, J. Tian, Z. Li, Q. Li, J. Chen, X. Hui, High temperature strengthening via nanoscale precipitation in wrought CoCrNi-based medium-entropy alloys, Mater. Sci. Eng. A 798 (2020) 140213, https://doi.org/10.1016/j.msea.2020.140213.
[78] N. Baler, A. Godha, S.K. Makineni, On the discontinuous precipitation during recrystallization in a multicomponent alloy, Scr. Mater. 224 (2023) 115133, https://doi.org/10.1016/j.scriptamat.2022.115133.
[79] J.Y.C. Fang, W.H. Liu, J.H. Luan, T. Yang, Y. Wu, M.W. Fu, Z.B. Jiao, Competition between continuous and discontinuous precipitation in L12-strengthened high-entropy alloys, Intermetallics 149 (2022) 107655, https://doi.org/10.1016/j.intermet.2022.107655.
[80] J.Y. He, H. Wang, H.L. Huang, X.D. Xu, M.W. Chen, Y. Wu, X.J. Liu, T.G. Nieh, K. An, Z.P. Lu, A precipitation-hardened high-entropy alloy with outstanding tensile properties, Acta Mater. 102 (2016) 187–196, https://doi.org/10.1016/j.actamat.2015.08.076.
[81] J.D. Nystrom, T.M. Pollock, W.H. Murphy, A. Garg, Discontinuous cellular precipitation in a high-refractory nickel-base superalloy, Metall. Mater. Trans. A 28 (1997) 2443–2452, https://doi.org/10.1007/s11661-997-0001-1.
[82] A. Heckl, S. Cenanovic, M. Göken, R.F. Singer, Discontinuous Precipitation and Phase Stability In Re- and Ru-Containing Nickel-Base Superalloys, Metall. Mater. Trans. A 43 (2012) 10–19, https://doi.org/10.1007/s11661-011-0833-6.
[83] T. Yang, Y.L. Zhao, L. Fan, J. Wei, J.H. Luan, W.H. Liu, C. Wang, Z.B. Jiao, J.J. Kai, C.T. Liu, Control of nanoscale precipitation and elimination of intermediate-temperature embrittlement in multicomponent high-entropy alloys, Acta Mater. 189 (2020) 47–59, https://doi.org/10.1016/j.actamat.2020.02.059.
[84] A.A.N. Németh, D.J. Crudden, D.E.J. Armstrong, D.M. Collins, K. Li, A. J. Wilkinson, C.R.M. Grovenor, R.C. Reed, Environmentally-assisted grain boundary attack as a mechanism of embrittlement in a nickel-based superalloy, Acta Mater. 126 (2017) 361–371, https://doi.org/10.1016/j.actamat.2016.12.039.
[85] J.X. Hou, S.F. Liu, B.X. Cao, J.H. Luan, Y.L. Zhao, Z. Chen, Q. Zhang, X.J. Liu, C. T. Liu, J.J. Kai, T. Yang, Designing nanoparticles-strengthened high-entropy alloys with simultaneously enhanced strength-ductility synergy at both room and elevated temperatures, Acta Mater. 238 (2022) 118216, https://doi.org/10.1016/j.actamat.2022.118216.
[86] K.S. Chan, A Grain Boundary Fracture Model for Predicting Dynamic Embrittlement and Oxidation-Induced Cracking in Superalloys, Metall. Mater. Trans. A 46 (2015) 2491–2505, https://doi.org/10.1007/s11661-015-2860-1.